

Hierarchy of Symmetry Breaking Correlated Phases in Twisted Bilayer Graphene

Robert Polski,^{1,2,*} Yiran Zhang,^{1,2,3,*} Yang Peng,⁴ Harpreet Singh Arora,^{1,2} Youngjoon Choi,^{1,2,3} Hyunjin Kim,^{1,2,3} Kenji Watanabe,⁵ Takashi Taniguchi,⁵ Gil Refael,^{2,3} Felix von Oppen,⁶ and Stevan Nadj-Perge^{1,2,†}

¹*T. J. Watson Laboratory of Applied Physics, California Institute of Technology, Pasadena, California 91125, USA*

²*Institute for Quantum Information and Matter, California Institute of Technology, Pasadena, California 91125, USA*

³*Department of Physics, California Institute of Technology, Pasadena, California 91125, USA*

⁴*Department of Physics and Astronomy, California State University, Northridge, California 91330, USA*

⁵*National Institute for Materials Science, Namiki 1-1, Tsukuba, Ibaraki 305 0044, Japan*

⁶*Dahlem Center for Complex Quantum Systems and Fachbereich Physik, Freie Universität Berlin, 14195 Berlin, Germany*

(Dated: May 12, 2022)

Twisted bilayer graphene (TBG) near the magic twist angle of $\sim 1.1^\circ$ exhibits a rich phase diagram. However, the interplay between different phases and their dependence on twist angle is still elusive. Here, we explore the stability of various TBG phases and demonstrate that superconductivity near filling of two electrons per moiré unit cell alongside Fermi surface reconstructions, as well as entropy-driven high-temperature phase transitions and linear-in-T resistance occur over a range of twist angles which extends far beyond those exhibiting correlated insulating phases. In the vicinity of the magic angle, we also find a metallic phase that displays a hysteretic anomalous Hall effect and incipient Chern insulating behaviour. Such a metallic phase can be rationalized in terms of the interplay between interaction-driven deformations of TBG bands leading to Berry curvature redistribution and Fermi surface reconstruction. Our results provide an extensive perspective on the hierarchy of correlated phases in TBG as classified by their robustness against deviations from the magic angle or, equivalently, their electronic interaction requirements.

TBG is a highly tunable platform for exploring the effects of strong electronic interactions and topological bands¹⁻⁹. At the magic angle, i.e., when the strength of the interactions among electrons is maximized relative to their kinetic energy, pronounced signatures of correlated phases emerge^{1,2,10}. Away from the magic angle, the effective interaction strength is reduced and the correlated phases are believed to disappear rapidly. However, despite the strong impact of the twist angle on the phase diagram of nearly-magic TBG, this dependence is still experimentally under-explored. Here we report systematic measurements on multiple devices covering a wide range of twist angles between 0.79° and 1.23° (see Supplementary Table I for an overview) and examine the overall impact of twist angle, and thus strength of interactions, on the phase

* These authors contributed equally to this work

† Correspondence: s.nadj-perge@caltech.edu

diagram of TBG.

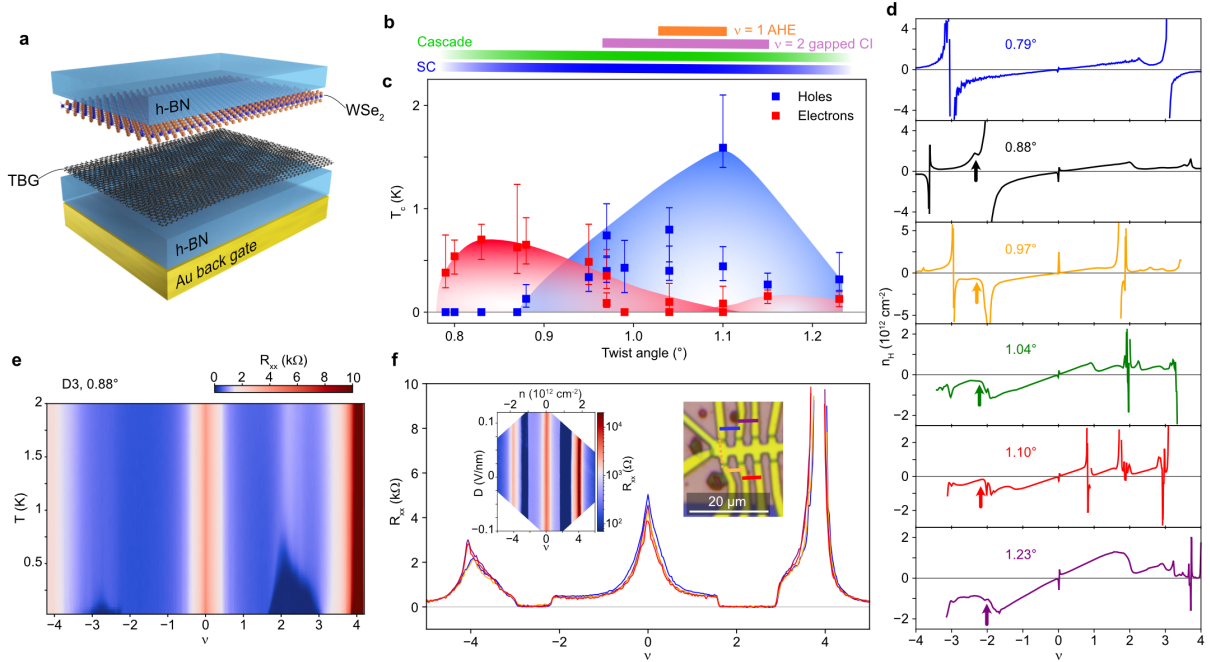


FIG. 1. Overview of the symmetry-broken phases and SC in TBG-WSe₂ for various twist angles. **a**, Schematic of the hexagonal boron nitride (hBN)-encapsulated TBG-WSe₂ structure with WSe₂ placed on top of TBG (see Methods for details of fabrication, comparison to TBG devices without WSe₂, and discussion of disorder). **b**, **c**, Phase diagram as a function of twist angle, indicating the regions which exhibit the AHE due to ferromagnetism, $\nu = +2$ correlated insulators (CI), superconductivity (SC), and symmetry breaking cascade effects as deduced from R_{xx} peaks and Hall density resets. The cascade and superconductivity start to disappear on either side of the diagram, as indicated by the fading bar color. **c**, Critical temperatures T_c of superconductivity for both holes and electrons over a range of twist angles between 0.79° and 1.23° (squares indicate 50% R_n and the error bars 10% and 90% R_n ; for more details, see Supplementary Fig. 2). The gradient-filled domes are guides to the eye. **d**, Hall density vs. moiré filling factor. Flavor symmetry breaking correlations manifest as Hall density resets (as seen clearly for 1.04° – 1.23° on the hole side, for instance, indicated by colored arrows) and occasionally as singularities or hole-like regions (as seen at 1.10° and 0.97° on the electron side). **e**, **f**, R_{xx} values measured for device D3, revealing the emerging hole-side superconductivity (**e**) and the uniformity of the sample over multiple contact pairs (**f**). The right inset of **f** shows contact pairs corresponding to the colors in the main plot, and the left inset shows that the device behavior is independent of a D field induced by a top gate in this device.

Figure 1a shows a schematic of the TBG-WSe₂ heterostructures (see Supplementary Fig. 1 and Methods for more details on device fabrication and the effects of WSe₂). We find correlated insulators with well defined activation gaps for twist angles in the relatively narrow range of 0.97° – 1.15° , indicating that the addition of WSe₂ leaves the value of the magic angle unaffected (Fig. 1b). Unlike the correlated insulators, we find that the cascade of high-temperature symmetry breaking transitions^{11,12} (discussed in more detail

below) and superconductivity near $\nu = \pm 2$ (where ν is the number of electrons per unit cell) persist over a much wider range of twist angles (Fig. 1b,c; see also Supplementary Fig. 2 and Ref. 5 for more data). While all devices exhibit pronounced electron-hole asymmetry and a peak T_c on the electron (hole) side which is shifted towards lower (higher) angles, superconductivity can be found well above ($\theta = 1.23^\circ$, D2) and below ($\theta = 0.88^\circ$, D3) the magic angle for both negative and positive filling factors (see Fig. 1c). To the best of our knowledge, this is the largest reported range of twist angles exhibiting superconductivity for both electron and hole doping.

Importantly, the observed superconducting regions are consistently accompanied by Fermi surface reconstructions around $\nu = \pm 2$, as manifested by a low-temperature reset in the Hall density. Consider, for example, the Hall density plots for the two lowest twist angles in Fig. 1d (blue and black curves). For 0.88° , hole-side SC around $\nu = -2$ has $T_c = 130$ mK and is accompanied by the formation of a kink in the Hall density (black arrow), which is separate from the van Hove singularity. At larger twist angles, the kink becomes a fully-developed Hall density reset to zero (colored arrows), corresponding to a more complete flavor symmetry breaking-induced Fermi surface reconstruction (see Supplementary Fig. 3 for more data). In contrast, the device with twist angle 0.79° reveals a linear Hall density on the hole side that extends well beyond $\nu = -2$, ultimately reaching a van Hove singularity¹³. This signals the absence of an interaction-driven Fermi surface reconstruction. Interestingly, we also no longer find hole-side superconductivity for this twist angle. On the electron side, both twist angles exhibit superconductivity and a kink in the Hall density due to Fermi surface reconstructions.

We note that the addition of WSe_2 , while not changing the magic angle value, may help stabilize superconductivity⁵ due to a reduction in disorder. We find in the best devices that four-point measurements almost perfectly overlap for different contact configurations (Fig. 1f), signaling high twist angle uniformity. Moreover, in a dual-gated geometry no dependence on the displacement field is found (Fig. 1f, inset). However, we note that typical schemes of assessing disorder such as estimating the full width at half-maximum near charge neutrality that work well for monolayer graphene do not correlate with the superconducting T_c or other disorder signatures in our samples (see methods and Supplementary Fig. 4).

Our observations indicate that a fully flavor (i.e., spin and valley) symmetric state strongly disfavors the formation of superconductivity. This rules out the simplest scenario for superconductivity based on electron-phonon coupling, which relies only on the local density of states¹⁴. Alternatively, and independently of the pairing mechanism, in the case of multiflavor pairing, superconductivity and magnetism (i.e., flavor polarization) can be inherently connected. This connection emerges from a simple energetic argument. If two flavors pair, they could increase their condensation energy by exchanging particles with the other flavors, such that they maximize their density of states. Roughly, this is captured through a term akin to $\Delta^2 M$ in the free energy, but with M (and Δ) being a matrix indicating the density of the various flavors on its diagonal, and correlations (pairing) in the off diagonal¹⁵. This term in the free energy implies that

strong flavor polarization (manifested in M) will generally increase the superconducting gap, and thus T_c , of a multflavor superconductor. Conversely, a finite superconducting order parameter could also induce polarization. Our experimental observation that enhanced superconductivity occurs only in regions with prominent Hall density resets is thus in line with multflavor pairing. This could potentially reconcile experiments with electron-phonon mechanisms of superconductivity, although we note that our results do not rule out unconventional mechanisms, based e.g., on flavor fluctuations¹⁶ or the Kohn-Luttinger scenario¹⁷.

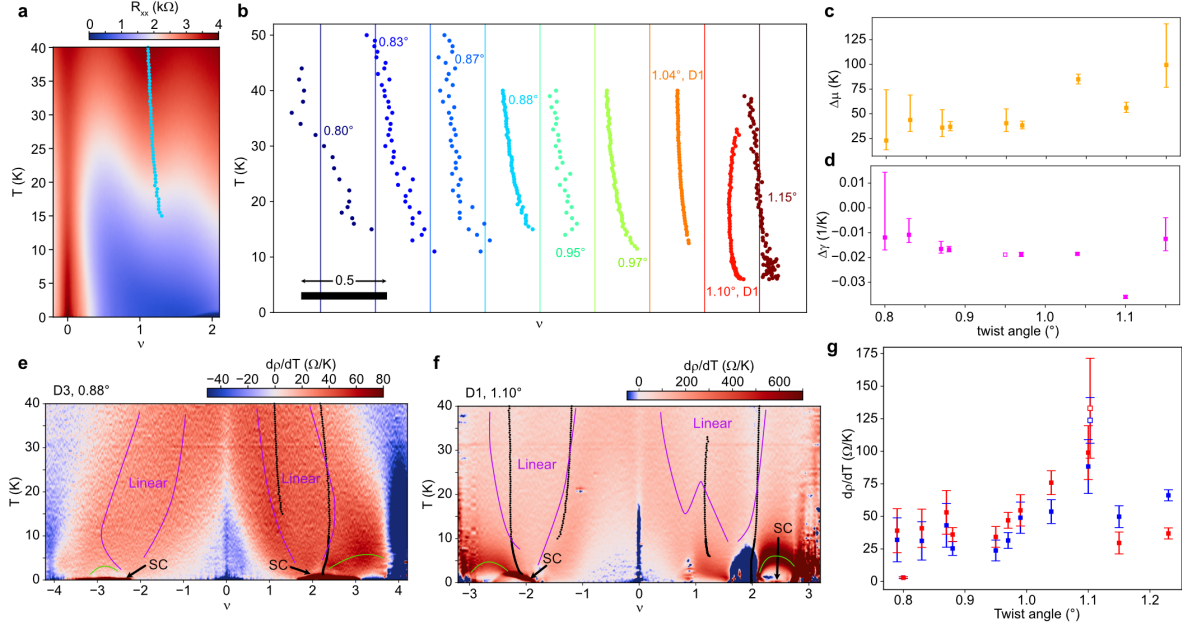


FIG. 2. Pomernanchuk-like phase transitions near $\nu = +1$ and linear T -dependence of resistivity. **a**, Example of a peak fit at $\nu \approx 1$ for a device at twist angle 0.88° . **b**, R_{xx} peak positions near filling factor $\nu \approx 1$ as a function of temperature for devices with various twist angles. The vertical colored lines represent the $\nu = 1$ filling factor for the respectively colored twist angle data. **c**, **d**, Fit parameters $\Delta\mu$ and $\Delta\gamma$ representing change in the chemical potential and specific heat (see Equation 1 in the Supplementary Information and Ref. 11) for the phase transition represented by the R_{xx} peaks in **b**. Error bars are 95% confidence intervals (the hollow square for 0.95° was set to the same $\Delta\gamma$ value as the 0.97° device due to the unconstrained $\Delta\gamma$ value for the data points). **e**, **f**, The derivative $\frac{d\rho}{dT}$ (where $\rho = R_{xx}W/L$ is the resistance scaled by the width W and length L of the sample) for devices at twist angles 0.88° and 1.10° , respectively. R_{xx} peaks corresponding to Pomernanchuk-like transitions are shown with black dots (corresponding to slight minima in $d\rho/dT$), superconductivity (SC) pockets are shown with arrows, and the magenta lines are guides to the eye representing the approximate regions of T -linear resistivity. The green lines reveal the inflection points under which low-temperature resistivity is super-linear. **g**, The resistivity slope $\frac{d\rho}{dT}$ for a range of twist angles, where red(blue) is for electrons(holes). The values come from the average derivative over the area spanned by $1.5 < \nu < 1.8$ ($-2 < \nu < -1.6$) for electrons (holes) and $15 < T < 38$ (error bars are the standard deviations). Device D4, twist angle 1.10° is represented by hollow squares.

The principal features emerging at higher temperatures (above 5–10 K), such as the cascade of phase

transitions between symmetry broken states near integer filling factors and the linear-in-T dependence of R_{xx} , are also present over a wide range of angles (Fig. 2 and Supplementary Fig. 2). In the case of $|\nu| \approx 1$, R_{xx} peaks are associated with a Pomeranchuk-like phase transition^{18,19} between a flavor symmetric state near charge neutrality and a symmetry broken phase with free local spin moments. The evolution of this phase boundary with temperature can be fit using a simple thermodynamic model including the entropy of localized spins¹⁹. The main parameters entering this model are the shift in the chemical potential $\Delta\mu$ due to the cascade transition and the change in specific heat $\Delta\gamma$ between the two phases.

Our data suggest that this description works reasonably well over the entire range of angles investigated here (Fig. 2a-d). Moreover, $\Delta\gamma$ appears to be roughly constant except for device D1 at 1.10° right at the magic angle, perhaps indicating additional correlation effects emerging for this angle. We note that this device also exhibits a metallic anomalous Hall phase near $\nu = 1$ at low temperatures, discussed below. The slowly increasing $\Delta\mu$ signals stronger shifts of the bands as the twist angle is increased, which is consistent with the reduction of the moiré length scale and thus stronger electronic interactions. The appearance of superconductivity, high-temperature symmetry breaking cascade transitions, and in particular Pomeranchuk-like transitions over similar twist angle ranges (see Supplementary Fig. 2 and Ref. 5 to see the fading cascade at the limits of twist angles studied here) suggests a possible connection between these instabilities and points to similarities between TBG and heavy-fermion systems²⁰ which also show rich phase diagrams exhibiting similar phases²¹⁻²³.

The twist angle dependence of the linear-in-T resistivity behavior is shown in Fig. 2e-g. A linear temperature dependence of the resistivity can be due to electron-phonon scattering, at least at higher temperatures (above 5–10K)²⁴⁻²⁶. Alternatively, this dependence has also been associated with strange metal behavior due to its onset at low temperatures and its strength near the $|\nu| = 2$ correlated phases^{8,27}. Our data show that the linear-in-T behavior is qualitatively similar in devices away from (Fig. 2e; see Supplementary Fig. 5 for more examples) and close to the magic angle (Fig. 2f). Both cases exhibit broad regions of linear-in-T behaviour fanning out from approximately $|\nu| = 2$ (delineated by magenta lines in Fig. 2e,f). At lower $|\nu|$, this region is bordered by a broad region near charge neutrality, where the increase in resistance is quadratic (consistent with expectations for Fermi liquid behaviour). At higher $|\nu| > 2$, there is a region where the temperature dependence of the resistivity crosses over from strongly super-linear to sub-linear as temperature increases. The intermediate inflection points, shown as green lines in Fig. 2e,f, appear to be intertwined with other TBG phases as they occasionally touch the superconducting domes (both for electrons and holes at 0.88° as well as for holes at 1.10°) or onset near $\nu \approx 2$, when a correlated insulating gap is present. This observation contrasts with the suggestion that the entire superconducting dome emerges below a linear-in-T phase²⁷. Note that both the magnitude of the T dependence (as measured by the slope near the green lines) and the linear-in-T slope measured at higher temperatures (within the magenta regions) are enhanced near the magic angle (Fig. 2g). This is to be expected, as the Fermi velocity is minimized for this angle and

could be even further reduced by interaction effects causing band flattening at nonzero filling²⁸. Finally we note that, in general, the linear-in-T slope peaks around the same angle value for both electrons and holes. This contrasts with the observed doping asymmetry of the twist angles at which the superconducting T_c becomes maximal, further highlighting the differences between high- and low-temperature symmetry breaking phenomena.

Now we focus on a magic-angle device with $\theta = 1.10^\circ$ (Fig. 3). Upon cooldown, this device exhibits clear R_{xx} peaks below $T \approx 40$ K at every integer $0 < |\nu| < 4$. As temperature is lowered further, a correlated insulator (CI) develops near $\nu = +2$, while other resistance peaks remain metallic or disappear gradually (Fig. 3a). For hole doping (Fig. 3b), the corresponding superconducting dome near $\nu = -2$ reaches a maximal transition temperature of $T_c = 1.6$ K, featuring vanishing longitudinal resistance R_{xx} and a Fraunhofer-like pattern in line with previously reported hBN-encapsulated, high-quality magic-angle TBG devices^{2-4,29,30} (see also Methods for more detailed information).

In contrast to the features at $\nu = \pm 2$, the evolution of R_{xx} near $\nu = \pm 1$ is more subtle. In the temperature range $6 \text{ K} < T < 40 \text{ K}$, the R_{xx} peaks near both $\nu = +1$ and $\nu = -1$ evolve towards lower filling factors $|\nu|$ as temperature increases, following the phase boundary discussed above (Fig. 3a,e). However, at lower temperatures, $T < 6 \text{ K}$, the two peaks show distinctly different behavior. While the hole-side peak completely disappears, reflecting simple metallic behavior from charge neutrality to $\nu \approx -2$, the peak near $\nu = 1$ gradually gives way to another peak emerging in the filling range $0.8 < \nu < 0.95$ that persists to the lowest temperatures (Fig. 3c). Careful inspection reveals that R_{xx} exhibits switching behavior around the peak, discontinuous resistance changes between the same sweep across ν taken at slightly different temperatures (Fig. 3d) presumably due to switching of domains. Further measurements in the ν and temperature range of this low-temperature R_{xx} peak reveal an anomalous Hall effect (AHE). Figure 3f shows hysteresis loops in the Hall resistance, R_{xy} , for $\nu = 0.9$ as measured from 0.3 K to 7 K. The loop has a coercive field of up to about 150 mT and is centered about zero magnetic field. The jump in resistance $\Delta R_{xy} = R_{xy}^{B_\uparrow} - R_{xy}^{B_\downarrow}$ reaches a maximal value of 2.5 k Ω , significantly smaller than the resistance quantum, which persists until the Curie temperature ~ 5 K (Fig. 3f inset). Signatures of an AHE phase are also observed at twist angles of 1.04° and 0.99° , as shown in Supplementary Fig. 8.

Importantly, the observed AHE phase appears well below filling factor $\nu = 1$, existing in the range $0.7 < \nu < 1$, with the maximal ΔR_{xy} occurring near $\nu = 0.88$ (Fig. 4a). Upon approaching $\nu = 0.95$, the filling at which R_{xx} peaks, the coercive field diverges accompanied by a sudden decrease in ΔR_{xy} . Then signatures of small hysteresis loops in the opposite direction appear (see Supplementary Fig. 7 for a more clear example). Additionally, hysteresis is observed when sweeping ν in opposite directions (Fig. 4b) and holding the magnetic field constant.

Measurements of R_{xy} at elevated temperatures and over a wider doping range further reveal the unusual nature of the observed AHE phase (Fig. 4c,d). Surprisingly, within the range of ν exhibiting the AHE and

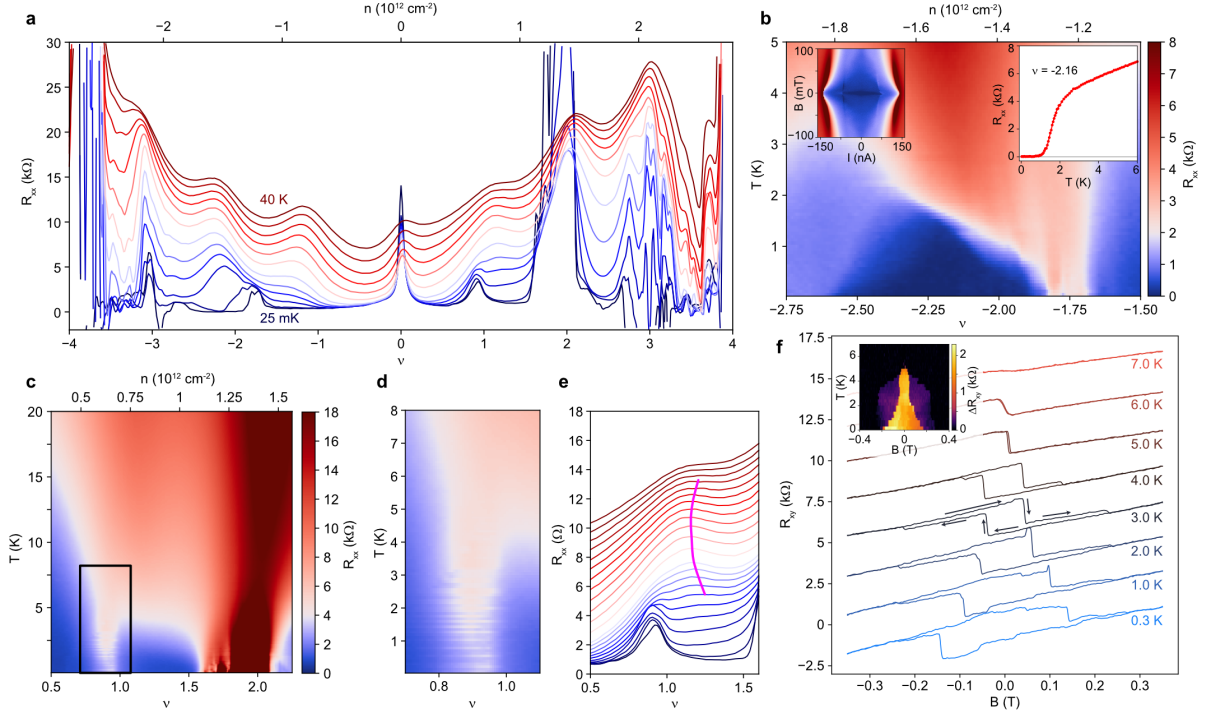


FIG. 3. Superconductivity and correlated states for a magic-angle TBG-WSe₂ device (D1). **a**, Line cuts of R_{xx} versus filling factor ν for a range of temperatures (shown is 25 mK, then 1, 3, 5, and 7 K, followed by every 5 K from 10 to 40 K). Superconductivity, correlated insulators, and orbital magnetism (incipient Chern insulator) emerge below 10K, whereas the symmetry breaking cascade transitions survive up to 40 K. **b**, R_{xx} versus temperature and filling factor on the hole side, showing a superconducting dome around $\nu = -2$. Insets, temperature dependence of R_{xx} at $\nu = -2.16$, showing the SC transition and Fraunhofer-like interference pattern ($\nu = -2.3$). **c**, R_{xx} versus temperature and filling factor focusing around $\nu = 1$. **d**, Zoom into the black box in **c**, revealing the switching behavior of the resistance, representative of the ferromagnetic state. **e**, Dense line-cut plots for the area around $\nu = 1$, showing that the evolution of R_{xx} maxima above 10 K (magenta line) are distinct from the ferromagnetic peak. These peaks mark the T-dependent cascade transition previously studied around filling factor one in TBG^{18,19}. **f**, Temperature dependence of R_{xy} versus B at $\nu = 0.90$ from 300 mK to 7 K. Successive curves are offset by 2.2 k Ω , and the arrows indicate the B field sweep directions. The inset demonstrates $\Delta R_{xy} = R_{xy}^{B_{\uparrow}} - R_{xy}^{B_{\downarrow}}$ versus B field and temperature at the same filling factor.

up to magnetic fields greater than 1 T, the sign of R_{xy} is opposite to that of the surrounding doping range. Also, R_{xy} changes sign when the temperature reaches ~ 5 K, consistent with the measured AHE Curie temperature. While naively this behaviour might be due to a change of carrier type from electrons to holes, the measurements show a linear increase in R_{xy} with increasing magnetic field throughout the entire doping range (Fig. 3f and Fig. 4e), consistent with dominant electron conduction.

The observation of hysteresis signals the emergence of an orbital ferromagnetic phase that arises from a band carrying nonzero Chern number $C^{31,32}$. A finite Chern number is also expected to result in R_{xy} and

R_{xx} features that follow the Streda formula in an out-of-plane magnetic field $B = \frac{h}{Ce}n$. We observe clear maxima and minima in R_{xx} approximately following the Streda formula at fields less than 3T (Fig. 4e), and specifically point to the R_{xx} minimum following $C = -1$ that extrapolates to $\nu = 0.95$ at zero field, near where the coercivity diverges. The low-field features disappear by $B = 3\text{--}4$ T, where a finite-field Chern insulating phase corresponding to $C = 3$ takes over. The observed switch in Chern number indicates the competing nature of these phases^{9,33}.

However, our observations stand in contrast to discussions of zero-field Chern insulators, where the chemical potential falls into an insulating gap^{9,33–35}. Throughout the entire doping range, the AHE phase observed here appears metallic. This is implied by the electron-like Hall resistivity and the finite R_{xx} peak at 0 T that is small compared to h/e^2 and increases with temperature. This contrasts with the expected vanishing of R_{xx} for a gapped bulk with gapless edge channels⁶ or a resistance $\sim h/e^2$ that can originate from domain walls extending between the contacts³⁶. We note that while disorder effects and the presence of domains observed in Ref.³⁵ can, to some extent, explain the absence of a gap and imperfect quantization, local compressibility^{11,37} and scanning tunneling spectroscopy measurements^{38,39} typically do not resolve a gapped state near $\nu = 1$. In the following, we present a scenario which would be consistent with the metallicity as well as the electron-like behaviour of R_{xy} in the AHE phase seen in Fig. 3f and Fig. 4e. Our scenario relies on the fact that strong interactions can heavily deform the TBG bands, such that the Γ point of the mini-Brillouin zone can be inverted, as reported by local spectroscopy measurements⁴⁰.

To model TBG, we employ a ten-band model⁴¹ that includes short-range Coulomb interactions⁴². First we show that this model, which uses a Hartree-Fock approximation, can capture the existence of the symmetry breaking cascade^{11,12} and TBG band structure deformations^{13,28,40,43} (see Supplementary Information for further discussion). Flavor-resolved mean-field band structures at $\nu = 0.81$ are shown in Fig. 4f,g. Here, the symmetry breaking cascade occurs well before ν reaches 1, with one of the spin-valley flavor bands being almost filled while the other three develop a gap and are shifted back to the vicinity of the charge neutrality point. Focusing on the three gapped bands, one can obtain a total Chern number of $C = \pm 3$ or $C = \pm 1$ ³³, depending on the exact symmetry breaking mechanism, when the chemical potential is within the gap. For example, broken \mathcal{T} symmetry naturally leads to $C = \pm 3$, and broken C_2 symmetry can give rise to $C = \pm 1$ phases³⁸.

Now consider the case displayed in Fig. 4g where the chemical potential for three flavors touches the bottom of the inverted electron pocket at the Γ point. Despite being slightly electron doped, the three flavors still contribute to the anomalous Hall conductance. Since the Berry curvature of the upper band is small near the bottom of the inverted electron pocket, as shown in Fig. 4i, the Chern number remains approximately conserved. The consistently positive slope $\frac{dR_{xy}}{dB}$ of the Hall resistivity arises from the electron-like bands of the barely filled flavors, while the apparent hole-like sign of R_{xy} originates from the negative offset caused by the anomalous Hall effect. The experimentally observed hysteresis, in this scenario, would

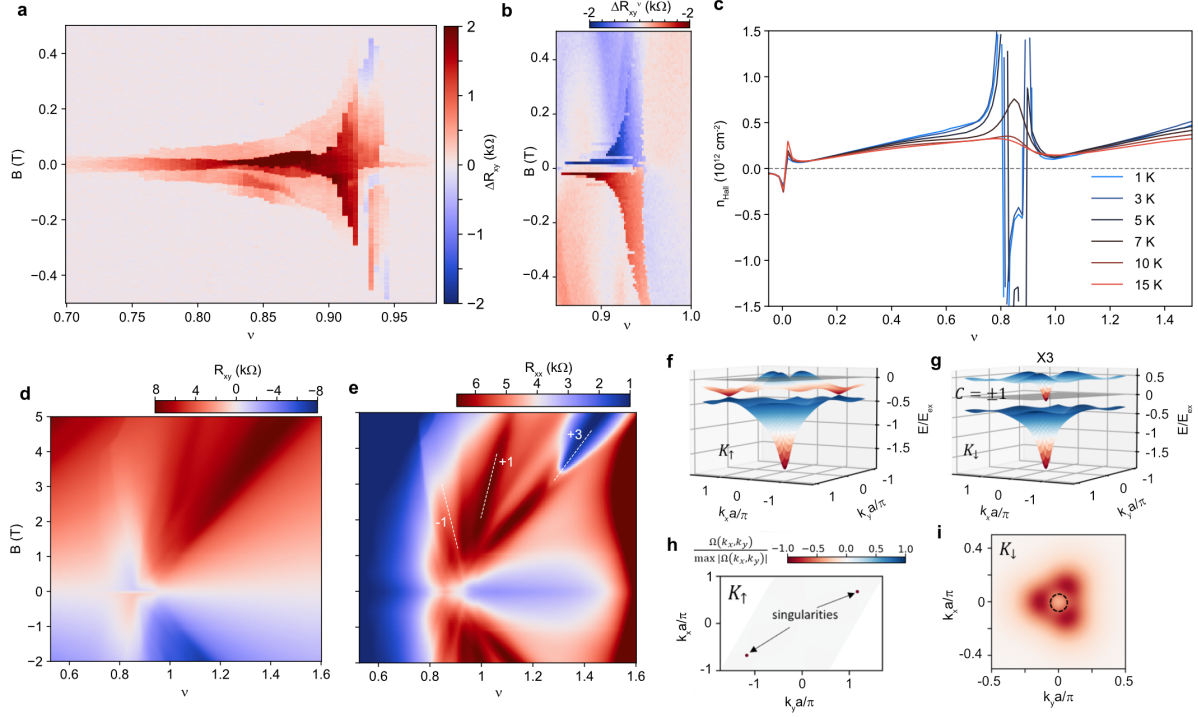


FIG. 4. Anomalous Hall effect and zero-field $C = -1$ correlated states near $\nu = 1$. **a**, ΔR_{xy} vs. B and ν around filling factor 1 measured at 1.5K. The divergence of the coercive field happens around $\nu = 0.95$. **b**, Hall density difference as a result of sweeping ν while holding magnetic field constant, $\Delta R_{xy}^\nu = R_{xy}^{\nu\uparrow} - R_{xy}^{\nu\downarrow}$. **c**, Hall density versus ν measured at 0.5T (the value shown is antisymmetrized $[R_{xy}(0.5T) - R_{xy}(-0.5T)]/2$) with temperature from 1K to 15K. n_{Hall} changes sign when entering the anomalous Hall region in (ν, T, B) parameter space, due to the AHE negative offset to R_{xy} as a result of the zero-field symmetry breaking. However, the slope of the R_{xy} vs. B measurements remain positive, as seen in **d** and Fig. 3f, meaning the overall behavior is still electron-like. **d**, **e**, Magnetic field and ν dependence of R_{xy} (**d**) and R_{xx} (**e**) around filling factor 1 measured at 3K. In addition to the $C = +3$ Chern insulator developed at high magnetic field, features associated with $C = \pm 1$ also emerge from filling factor 1, as labeled in **e**. The origin of the $C = -1$ line is at $\nu = 0.94$, indicating that an incipient Chern insulator $C = -1$ is responsible for anomalous Hall signal observed around $\nu = 1$. **f**, **g**, The band structure obtained for each spin and mini-valley (K, K') flavor from the 10-band model for the case of broken $C_2\mathcal{T}$ symmetry at $\nu \simeq 0.81$. The K_\uparrow flavor, which is nearly filled, preserves the Dirac-like band structure (**f**), whereas the other three flavors have a $C_2\mathcal{T}$ -broken mass (**g**). The gray planes represent the chemical potential. Here we assume the mass term is invariant under \mathcal{T} operation, which gives overall Chern number $C = \pm 1$. **h**, **i**, Berry curvature Ω_{k_x, k_y} for the conduction flat band in the K_\uparrow flavor (**h**) and for K_\downarrow (**i**), where the Berry curvature is concentrated above the Γ pocket. The Fermi surface is plotted as a dotted circle. The other two flavors, from the opposite valley K' , have the same Berry curvature as **i** but opposite sign.

still be explained by orbital ferromagnetism³¹. Due the metallic nature of the system, the Streda formula with $C = -1; \nu = 1$ at $B = 0$ T is only approximately satisfied. We note, that while the mean-field calculations presented here successfully capture a possible metallic AHE phase, other ground states with similar characteristics may also be possible^{13,33,44,45} and are hard to rule out based on our data. Finally similar scenario to the one proposed here can also explain AHE phases observed recently near $\nu = \pm 2$ ^{46,47}.

Our results show that the robustness to deviations of the twist angle from the magic angle divides TBG phases into two categories. Superconductivity, cascade transitions, as well as the linear-in-T dependence of the resistivity are robust over a wide range of twist angles, spanning at least $0.8^\circ \lesssim \theta \lesssim 1.23^\circ$. Moreover, the cascade transitions near $\nu = \pm 2$ appear to be a necessary prerequisite for the appearance of superconductivity, implying close relations between these two phases. In contrast, the correlated insulating and orbital ferromagnetic states require a more subtle interplay of strong interactions, kinetic energy scales, and possible breaking of spatial symmetries. Due to this sensitivity, these phases appear in a more immediate vicinity of the magic angle, where the close competition between various phases can result in differing behaviour of devices with the same twist angle (e.g., see Supplementary Fig. 6). This hierarchy of TBG phases will guide future theoretical frameworks aiming to explain the rich phenomenology of TBG and related structures.

METHODS

Device Fabrication: The devices were fabricated using a ‘cut and stack’ method, in which graphene flakes were separated into two pieces using a sharp Platinum-Iridium tip; this prevents unwanted twisting and strain during tearing while allowing more control over the flake size and shape. First, a thin hBN flake (10–30 nm) is picked up using a propylene carbonate film (PC) previously placed on a polydimethylsiloxane (PDMS) stamp. Then the hBN is used to pick up an exfoliated monolayer of WSe₂ (commercial source, HQ graphene) before approaching the graphene. After picking up the first half of the graphene flake, the transfer stage is rotated by approximately 1.1–1.3° (overshooting the target angle slightly), and then the second half is picked up, forming the twisted bilayer. Care was taken to approach and pick up each stacking step slowly. In the last step, a thicker hBN (30–70 nm) is picked up, and the whole stack is dropped on a predefined local gold back-gate at 150° C while the PC is released at 170° C. The PC is then cleaned off with N-Methyl-2-Pyrrolidinone (NMP). The final geometry is defined by dry etching with a CHF₃/O₂ plasma and deposition of ohmic edge contacts (Ti/Au, 5 nm/100 nm).

Measurements: All measurements were performed in a dilution refrigerator (Oxford Triton) with a base temperature of ~ 25 mK, using standard low-frequency lock-in amplifier techniques. Unless otherwise specified, measurements are taken at the base temperature. Frequencies of the lock-in amplifiers (Stanford Research, models 830 and 865a) were kept in the range of 7–20 Hz in order to measure the device’s DC

properties and the AC excitation was kept <5 nA (most measurements were taken at 0.5–1 nA to preserve the linearity of the system and avoid disturbing the fragile states at low temperatures). Each of the DC fridge lines pass through cold filters, including 4 Pi filters that filter out a range from ~ 80 MHz to >10 GHz, as well as a two-pole RC low-pass filter.

Similarities to hBN-encapsulated samples: Here we briefly discuss similarities between devices studied here and hBN-encapsulated devices. While we showed previously that WSe₂ induces some amount of spin-orbit coupling⁵, it does not change the magic angle significantly since both the most prominent correlated insulating states at $\nu = +2$ and highest T_c -superconductivity are observed near 1.1° . Moreover, the trends of metallic resistance peaks at high temperature (Supplementary Fig. 2) and the gaps between the flat and dispersive bands are consistent with hBN-encapsulated devices²⁵. Note that the samples showing similar full-filling gaps likely have the same ratio between the tunneling energies on AA sites and AB sites (often represented as w_{AA}/w_{AB} in the continuum model)⁴⁸. In this context, our main finding is that adding a WSe₂ layer decreases the amount of twist angle disorder on the hundreds-of-nanometer to μm scale in devices, as confirmed separately by STM measurements³⁹. This finding is also consistent with our four point measurements for some of our best devices (see for example Fig. 1f). Another sign of decreased disorder is found in the well developed R_{xy} plateaus at relatively low magnetic fields in our devices⁵ (see also Supplementary Fig. 6). This may explain our observation, in part, of superconductivity over a large angle range although the spin-orbit coupling may still play a role, particularly in the electron-side superconductivity away from the magic angle where hBN encapsulated TBG data is lacking and comparison is not possible.

Disorder in TBG-WSe₂ devices: In all TBG devices studied so far, it appears that there are significant device-to-device variations that are often associated with disorder. In addition to disorder that is intrinsic to graphene (such as charge disorder originating from residual polymers and other impurities, disordered edges, strain from wrinkles or bubbles, strain from the substrate or back gate), in TBG twist angle disorder is believed to play an important role. As previously reported, it generates domains and gradual twist-angle shifts on length scales from 100 nm to a micron^{39,49}. In this context, characterizing TBG disorder through transport measurements is somewhat more elusive as transport averages over device length scales (a few μm). It is important to emphasize that measurements of disorder that are typically used in a single layer of graphene and commonly detected through broadening of charge-neutrality peaks in longitudinal or Hall resistance (full width at half max—FWHM—of R_{xx}), do not correlate well with superconductivity or other features that may point towards disorder in the TBG samples (Fig. 1g).

Occasionally, we see evidence in transport of the presence of domains with slightly different twist angles (on the scale of the contact separation, or slightly smaller, a few hundred nm to a few μm), resulting in multiple resistance features near $\nu = 2$ (Supplementary Fig. 9d), and a Landau fan diagram that is not as distinct as other devices. Other devices show variation in the twist angle over a range of contact pairs (length scales 2-20 μm , see Supplementary Table I) but still show less disorder in fan diagrams and strong

correlations for each individual pair of contacts, owing likely to large domains.

In the least disordered devices (in the context of transport measurements), the global twist-angle deviation between different contact pairs is below the detectable limit. For instance, Fig. 1f shows a device with longitudinal resistance traces that almost exactly match over four pairs of contacts. This device, made with Au top and back gates and a monolayer of WSe₂ on top of the TBG, also shows uniform resistance and superconducting features over the applicable electric displacement field D range (Fig. 1f, inset). This suggests a low disorder as probed by D -field asymmetry that occurs in some previous hBN encapsulated devices³. The D -invariant superconductivity also implies that the substrate asymmetry introduced by WSe₂ is minimal, at least for twist angle of 0.88°. Moreover, we note that different contact pairs in this study are checked in a four-point measurement configuration (the standard used for measuring correlated states such as SC) and cross-checked with temperature dependence and magnetic field dependence for extraneous features, a process we find is more sensitive to disorder compared to the verification of twist angle disorder using two point measurements performed previously on hBN encapsulated devices. Further work (both in theory and experiment) is needed for more precise characterization of the role of disorder in TBG devices.

-
- [1] Y. Cao, V. Fatemi, A. Demir, S. Fang, S. L. Tomarken, J. Y. Luo, J. D. Sanchez-Yamagishi, K. Watanabe, T. Taniguchi, E. Kaxiras, R. C. Ashoori, and P. Jarillo-Herrero, *Nature* **556**, 80 (2018).
 - [2] Y. Cao, V. Fatemi, S. Fang, K. Watanabe, T. Taniguchi, E. Kaxiras, and P. Jarillo-Herrero, *Nature* **556**, 43 (2018).
 - [3] M. Yankowitz, S. Chen, H. Polshyn, Y. Zhang, K. Watanabe, T. Taniguchi, D. Graf, A. F. Young, and C. R. Dean, *Science* **363**, 1059 (2019).
 - [4] X. Lu, P. Stepanov, W. Yang, M. Xie, M. A. Aamir, I. Das, C. Urgell, K. Watanabe, T. Taniguchi, G. Zhang, A. Bachtold, A. H. MacDonald, and D. K. Efetov, *Nature* **574**, 653 (2019).
 - [5] H. S. Arora, R. Polski, Y. Zhang, A. Thomson, Y. Choi, H. Kim, Z. Lin, I. Z. Wilson, X. Xu, J.-H. Chu, K. Watanabe, T. Taniguchi, J. Alicea, and S. Nadj-Perge, *Nature* **583**, 379 (2020).
 - [6] M. Serlin, C. L. Tschirhart, H. Polshyn, Y. Zhang, J. Zhu, K. Watanabe, T. Taniguchi, L. Balents, and A. F. Young, *Science* **367**, 900 (2019).
 - [7] A. L. Sharpe, E. J. Fox, A. W. Barnard, J. Finney, K. Watanabe, T. Taniguchi, M. A. Kastner, and D. Goldhaber-Gordon, *Science* **365**, 605 (2019).
 - [8] Y. Cao, D. Chowdhury, D. Rodan-Legrain, O. Rubies-Bigorda, K. Watanabe, T. Taniguchi, T. Senthil, and P. Jarillo-Herrero, *Physical Review Letters* **124**, 076801 (2020), arXiv:1901.03710.
 - [9] P. Stepanov, M. Xie, T. Taniguchi, K. Watanabe, X. Lu, A. H. MacDonald, B. A. Bernevig, and D. K. Efetov, arXiv:2012.15126 [cond-mat] (2020), arXiv:2012.15126 [cond-mat].
 - [10] R. Bistritzer and A. H. MacDonald, *Proceedings of the National Academy of Sciences* **108**, 12233 (2011).
 - [11] U. Zondiner, A. Rozen, D. Rodan-Legrain, Y. Cao, R. Queiroz, T. Taniguchi, K. Watanabe, Y. Oreg, F. von Oppen, A. Stern, E. Berg, P. Jarillo-Herrero, and S. Ilani, *Nature* **582**, 203 (2020).
 - [12] D. Wong, K. P. Nuckolls, M. Oh, B. Lian, Y. Xie, S. Jeon, K. Watanabe, T. Taniguchi, B. A. Bernevig, and

- A. Yazdani, *Nature* **582**, 198 (2020).
- [13] M. Xie and A. H. MacDonald, arXiv:2010.07928 [cond-mat] (2020), arXiv:2010.07928 [cond-mat].
- [14] W. Qin, B. Zou, and A. H. MacDonald, arXiv:2102.10504 [cond-mat] (2021), arXiv:2102.10504 [cond-mat].
- [15] R. W. Cherng, G. Refael, and E. Demler, *Physical Review Letters* **99**, 130406 (2007).
- [16] Y.-Z. You and A. Vishwanath, *npj Quantum Materials* **4**, 1 (2019).
- [17] J. González and T. Stauber, *Physical Review Letters* **122**, 026801 (2019).
- [18] Y. Saito, F. Yang, J. Ge, X. Liu, T. Taniguchi, K. Watanabe, J. I. A. Li, E. Berg, and A. F. Young, *Nature* **592**, 220 (2021).
- [19] A. Rozen, J. M. Park, U. Zondiner, Y. Cao, D. Rodan-Legrain, T. Taniguchi, K. Watanabe, Y. Oreg, A. Stern, E. Berg, P. Jarillo-Herrero, and S. Ilani, *Nature* **592**, 214 (2021), arXiv:2009.01836.
- [20] Z.-D. Song and B. A. Bernevig, arXiv:2111.05865 [cond-mat] (2021), arXiv:2111.05865 [cond-mat].
- [21] G. R. Stewart, *Reviews of Modern Physics* **56**, 755 (1984).
- [22] G. Lonzarich, D. Pines, and Y.-f. Yang, *Reports on Progress in Physics* **80**, 024501 (2016).
- [23] M. A. Continentino and A. S. Ferreira, *Physical Review B* **69**, 233104 (2004).
- [24] F. Wu, E. Hwang, and S. Das Sarma, *Physical Review B* **99**, 165112 (2019).
- [25] H. Polshyn, M. Yankowitz, S. Chen, Y. Zhang, K. Watanabe, T. Taniguchi, C. R. Dean, and A. F. Young, *Nature Physics* **15**, 1011 (2019).
- [26] S. D. Sarma and F. Wu, arXiv:2201.10270 [cond-mat] (2022), arXiv:2201.10270 [cond-mat].
- [27] A. Jaoui, I. Das, G. Di Battista, J. Díez-Mérida, X. Lu, K. Watanabe, T. Taniguchi, H. Ishizuka, L. Levitov, and D. K. Efetov, arXiv:2108.07753 [cond-mat] (2022), arXiv:2108.07753 [cond-mat].
- [28] Z. A. H. Goodwin, V. Vitale, X. Liang, A. A. Mostofi, and J. Lischner, *Electronic Structure* **2**, 034001 (2020), arXiv:2004.14784.
- [29] Y. Saito, J. Ge, K. Watanabe, T. Taniguchi, and A. F. Young, *Nature Physics* **16**, 926 (2020).
- [30] P. Stepanov, I. Das, X. Lu, A. Fahimniya, K. Watanabe, T. Taniguchi, F. H. L. Koppens, J. Lischner, L. Levitov, and D. K. Efetov, *Nature* **583**, 375 (2020).
- [31] J. Zhu, J.-J. Su, and A. H. MacDonald, *Physical Review Letters* **125**, 227702 (2020).
- [32] H. Polshyn, J. Zhu, M. A. Kumar, Y. Zhang, F. Yang, C. L. Tschirhart, M. Serlin, K. Watanabe, T. Taniguchi, A. H. MacDonald, and A. F. Young, *Nature* **588**, 66 (2020).
- [33] B. Lian, Z.-D. Song, N. Regnault, D. K. Efetov, A. Yazdani, and B. A. Bernevig, *Physical Review B* **103**, 205414 (2021).
- [34] J.-X. Lin, Y.-H. Zhang, E. Morissette, Z. Wang, S. Liu, D. Rhodes, K. Watanabe, T. Taniguchi, J. Hone, and J. I. A. Li, arXiv:2102.06566 [cond-mat] (2021), arXiv:2102.06566 [cond-mat].
- [35] S. Grover, M. Bocarsly, A. Uri, P. Stepanov, G. Di Battista, I. Roy, J. Xiao, A. Y. Meltzer, Y. Myasoedov, K. Pareek, K. Watanabe, T. Taniguchi, B. Yan, A. Stern, E. Berg, D. K. Efetov, and E. Zeldov, arXiv:2201.06901 [cond-mat] (2022), arXiv:2201.06901 [cond-mat].
- [36] H. Polshyn, Y. Zhang, M. A. Kumar, T. Soejima, P. Ledwith, K. Watanabe, T. Taniguchi, A. Vishwanath, M. P. Zaletel, and A. F. Young, arXiv:2104.01178 [cond-mat] (2021), arXiv:2104.01178 [cond-mat].
- [37] J. Yu, B. A. Foutty, Z. Han, M. E. Barber, Y. Schattner, K. Watanabe, T. Taniguchi, P. Phillips, Z.-X. Shen, S. A. Kivelson, and B. E. Feldman, arXiv:2108.00009 [cond-mat] (2021), arXiv:2108.00009 [cond-mat].
- [38] K. P. Nuckolls, M. Oh, D. Wong, B. Lian, K. Watanabe, T. Taniguchi, B. A. Bernevig, and A. Yazdani, *Nature*

- 588, 610 (2020).
- [39] Y. Choi, H. Kim, Y. Peng, A. Thomson, C. Lewandowski, R. Polski, Y. Zhang, H. S. Arora, K. Watanabe, T. Taniguchi, J. Alicea, and S. Nadj-Perge, *Nature* **589**, 536 (2021).
- [40] Y. Choi, H. Kim, C. Lewandowski, Y. Peng, A. Thomson, R. Polski, Y. Zhang, K. Watanabe, T. Taniguchi, J. Alicea, and S. Nadj-Perge, *Nature Physics* **17**, 1375 (2021).
- [41] H. C. Po, L. Zou, T. Senthil, and A. Vishwanath, *Physical Review B* **99**, 195455 (2019).
- [42] Y. Choi, J. Kemmer, Y. Peng, A. Thomson, H. Arora, R. Polski, Y. Zhang, H. Ren, J. Alicea, G. Refael, F. von Oppen, K. Watanabe, T. Taniguchi, and S. Nadj-Perge, *Nature Physics* **15**, 1174 (2019).
- [43] T. Cea and F. Guinea, *Physical Review B* **102**, 045107 (2020).
- [44] Y. H. Kwan, G. Wagner, T. Soejima, M. P. Zaletel, S. H. Simon, S. A. Parameswaran, and N. Bultinck, arXiv:2105.05857 [cond-mat] (2021), arXiv:2105.05857 [cond-mat].
- [45] G. Shavit, E. Berg, A. Stern, and Y. Oreg, arXiv:2107.08486 [cond-mat] (2021), arXiv:2107.08486 [cond-mat].
- [46] C.-C. Tseng, X. Ma, Z. Liu, K. Watanabe, T. Taniguchi, J.-H. Chu, and M. Yankowitz, arXiv:2202.01734 [cond-mat] (2022), arXiv:2202.01734 [cond-mat].
- [47] J.-X. Lin, Y.-H. Zhang, E. Morissette, Z. Wang, S. Liu, D. Rhodes, K. Watanabe, T. Taniguchi, J. Hone, and J. I. A. Li, *Science* **375**, 437 (2022).
- [48] N. N. T. Nam and M. Koshino, *Physical Review B* **96**, 075311 (2017).
- [49] A. Uri, S. Grover, Y. Cao, J. A. Crosse, K. Bagani, D. Rodan-Legrain, Y. Myasoedov, K. Watanabe, T. Taniguchi, P. Moon, M. Koshino, P. Jarillo-Herrero, and E. Zeldov, *Nature* **581**, 47 (2020).

Acknowledgments: We acknowledge discussions with Cyprian Lewandowski, Jason Alicea, and Alex Thomson. **Funding:** This work has been primarily supported by the DOE-QIS program (DE-SC0019166) and NSF-CAREER (DMR-1753306). S.N-P. acknowledges support from the Sloan Foundation. G.R. and S.N.-P. also acknowledge the support of the Institute for Quantum Information and Matter, an NSF Physics Frontiers Center with support of the Gordon and Betty Moore Foundation through Grant GBMF1250; Y.P. acknowledges support from the startup fund from California State University, Northridge. F.v.O. is supported by Deutsche Forschungsgemeinschaft within CRC 183 (project C02) as well as the project TWIST-GRAPH.

Author Contribution: R.P. and Y.Z. performed the measurements, fabricated devices, and analyzed the data. H.P., Y.C., and H.K. helped with device fabrication and data analysis. Y. P. developed a theoretical model and performed model calculations in close collaboration with F.v.O. and G.R. K.W., and T.T. provides hBN crystals. S.N-P. supervised the project. R.P, Y.Z. Y.P., F.v.O. G.R. and S.N-P. wrote the manuscript with the input of other authors.

Competing interests: The authors declare no competing interests.

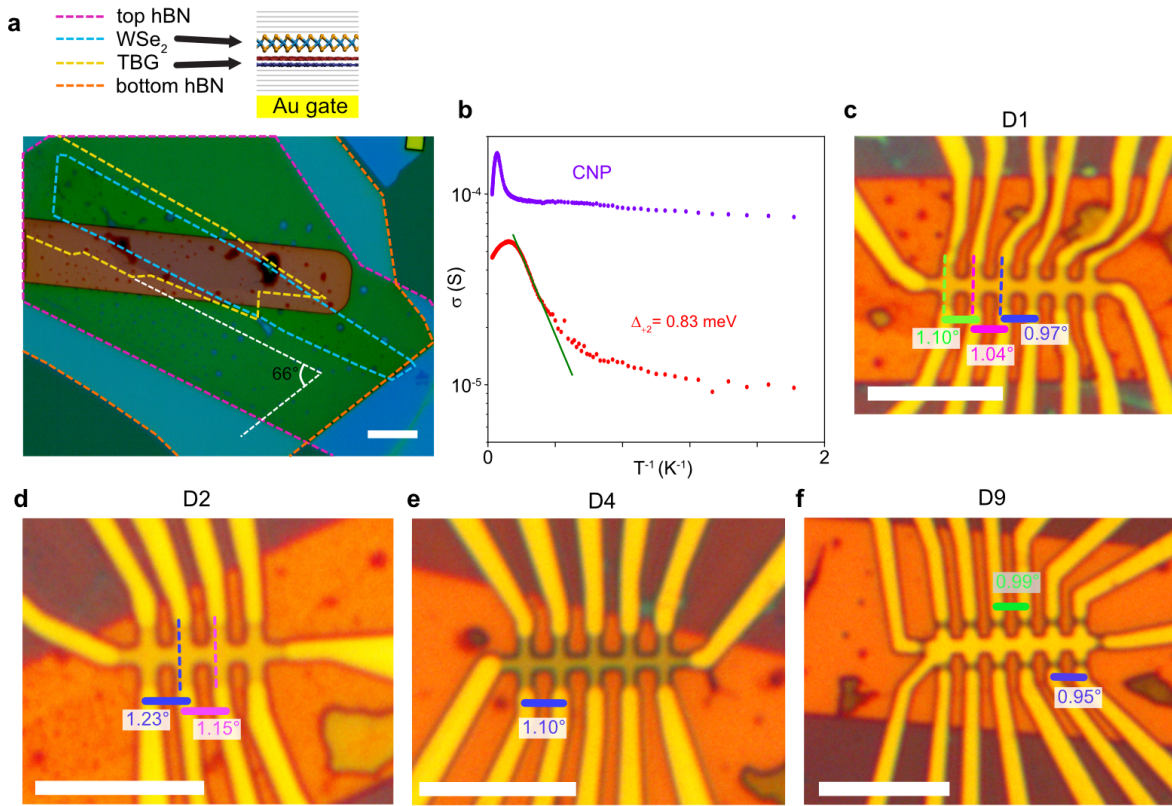
Data availability: The data that support the findings of this study are available from the corresponding authors on reasonable request.

Code availability: The code that support the findings of this study are available from the corresponding authors on reasonable request.

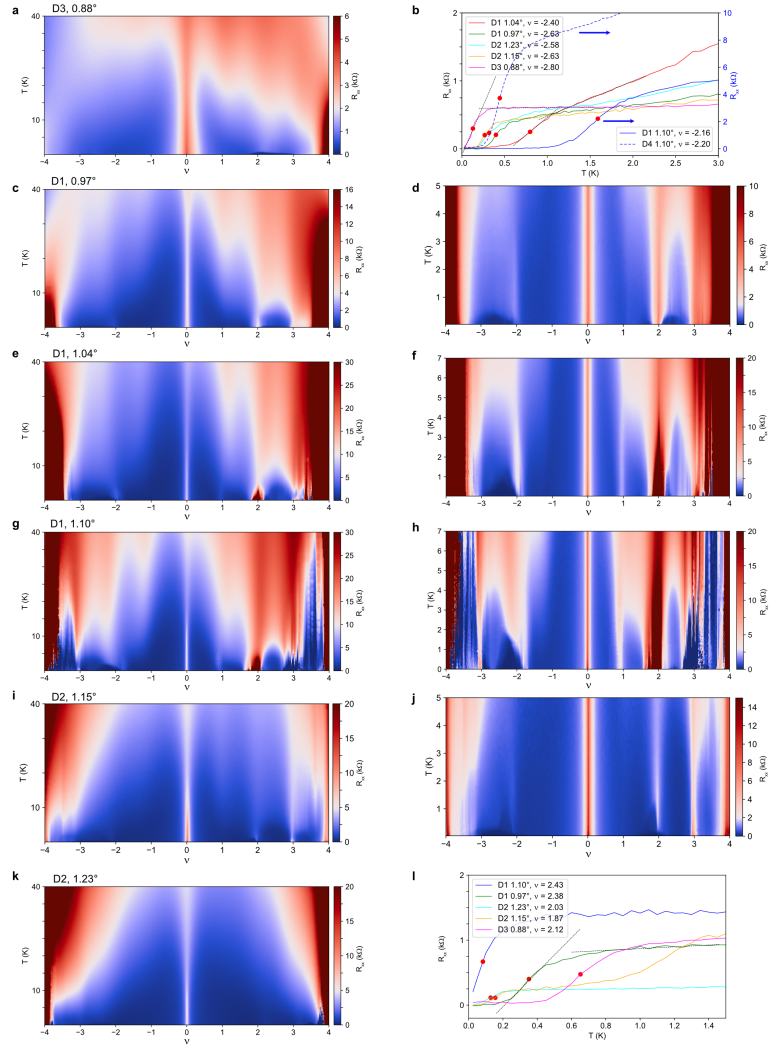
**SUPPLEMENTARY INFORMATION: HIERARCHY OF
SYMMETRY BREAKING CORRELATED PHASES
IN TWISTED BILAYER GRAPHENE**

Robert Polski, Yiran Zhang, Yang Peng, Harpreet Singh Arora, Youngjoon Choi, Hyunjin Kim, Kenji Watanabe,
Takashi Taniguchi, Gil Refael, Felix von Oppen, and Stevan Nadj-Perge

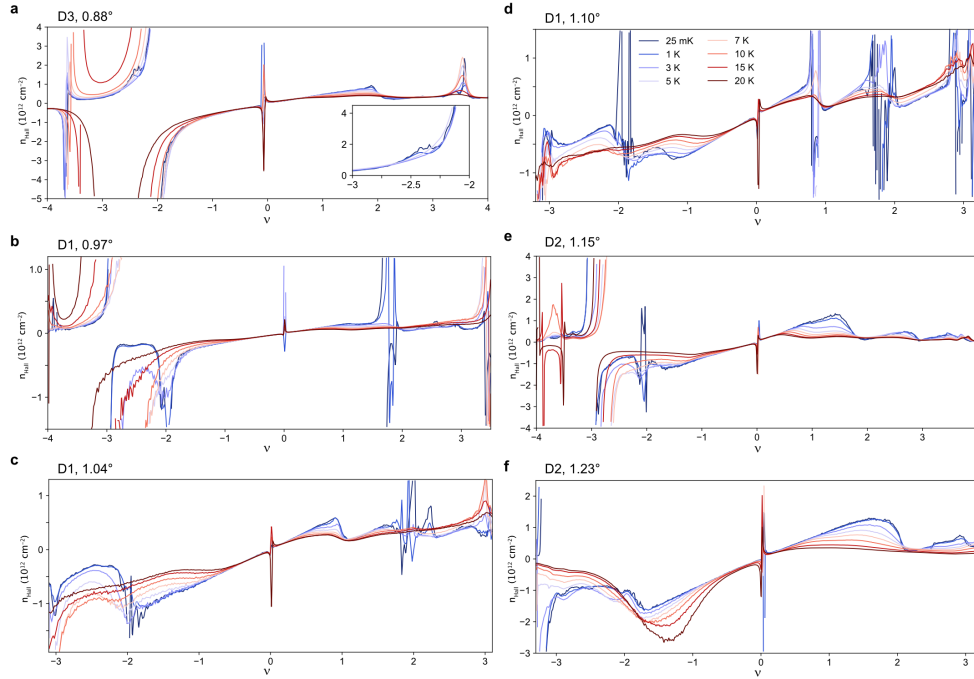
Experiment: Supplementary figures and the overview table



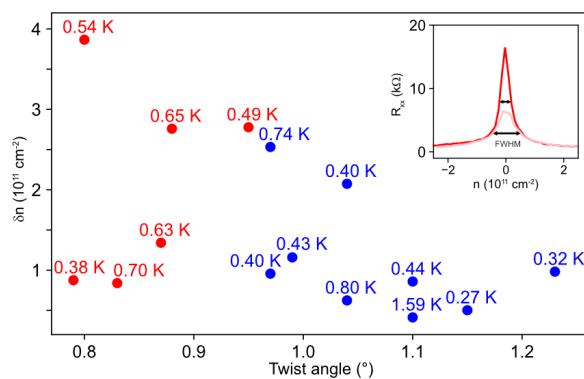
Supplementary Figure 1. **Optical images of devices and correlated gap analysis.** **a**, An optical image of D1 TBG-WSe₂ heterostructure with different layers delineated by dashed lines with different colors. The angle between graphene and bottom hBN edges is $\sim 66^\circ$, showing no obvious alignment. **b**, Conductance versus $1/T$ for charge neutrality and partial filling factor $\nu = 2$ from the data in Fig. 3a. The green line and the gap value shown are extracted from the activation fit, to the form $\sigma \propto e^{-\Delta/2k_B T}$. In contrast, the conductance at charge neutrality shows a much smaller variation in temperature without a clear activated gap. **c-f**, Optical images of devices used in the study. Bold colored lines show contact pairs used for R_{xx} measurements (and corresponding measured twist angles), while dashed colored lines show contact pairs used for R_{xy} measurements. White scale bars represent $10 \mu\text{m}$. For images of other devices in Supplementary Table I, see Ref. 5.



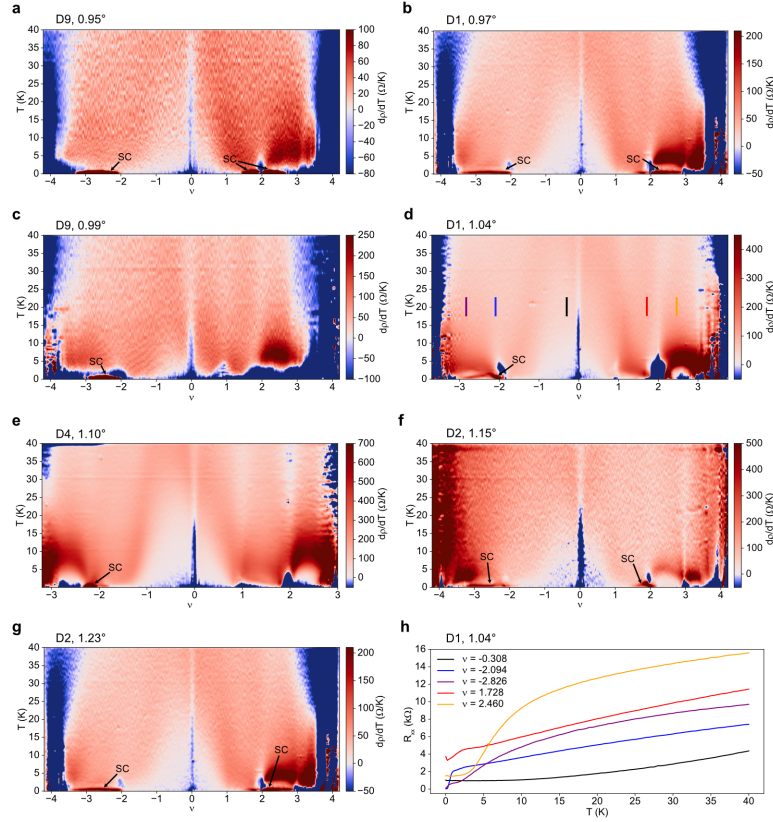
Supplementary Figure 2. **Temperature dependence in a collection of devices.** Figures in the left column show the high-temperature (to 40 K) R_{xx} vs. the moiré filling factor for a number of devices across the angle range. The corresponding figures in the right column reduce the temperature range to emphasize the correlated insulators and superconductivity appearing at low temperature. **b** shows extracted T_c on the hole side for each of the angles represented here. The resistance was much larger for device D1 at 1.10° , as well as another device D4 at the same twist angle, so the y-axis for these curves is on the right of the plot. The extreme sensitivity of the correlations and superconductivity to the twist angle, cleanliness, homogeneity, and other factors occasionally results in different T_c values for devices of the same angle. **i**, The electron-side superconductivity T_c values. T_c was derived from 50% R_n , where R_n is defined as the intersection of line fits to the highly sloped region and the normal region just above the transition (line fits shown for selected curves as dashed black lines). The same method was used to determine the error-bars at 10% and 90% R_n in Fig. 1c.



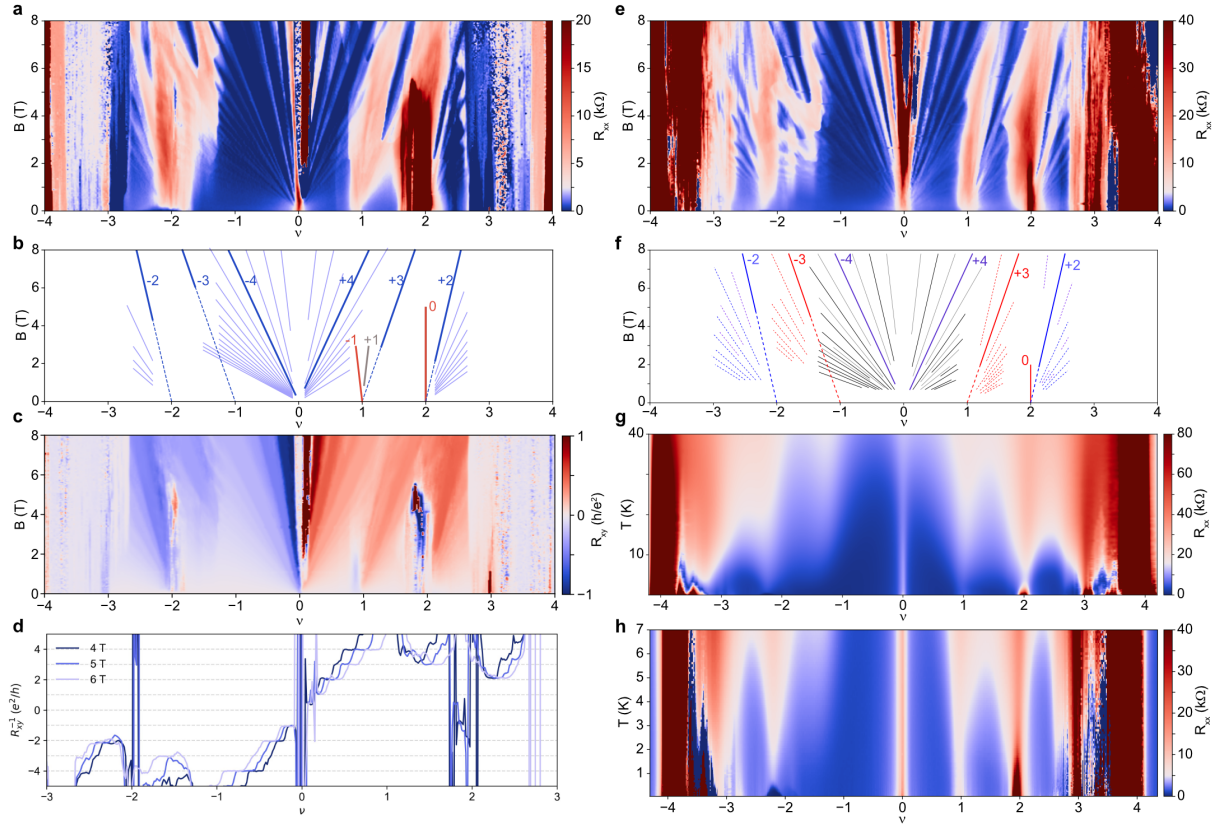
Supplementary Figure 3. **Cascade behavior Hall density measurements at select temperatures.** More detailed Hall density data for the mentioned devices, taken at the the range of temperatures displayed in **b**. The only deviation from these panels is in **a**, where the lowest-temperature curve was measured at 50 mK instead of 25 mK. The inset of **a** displays the $\nu \approx -2$ region for the 0.88° device as it evolves at temperatures up to 5 K, revealing the appearance of the feature mentioned in the main text and Fig. 1d, which corresponds with the onset of hole-side superconductivity. This small feature, indicative of the onset of a cascade, survives to only around 2 K. The rest of the panels reveal clear cascades, where the Hall density returns to near 0, at both $\nu = -2$ and $+2$ at low temperatures.



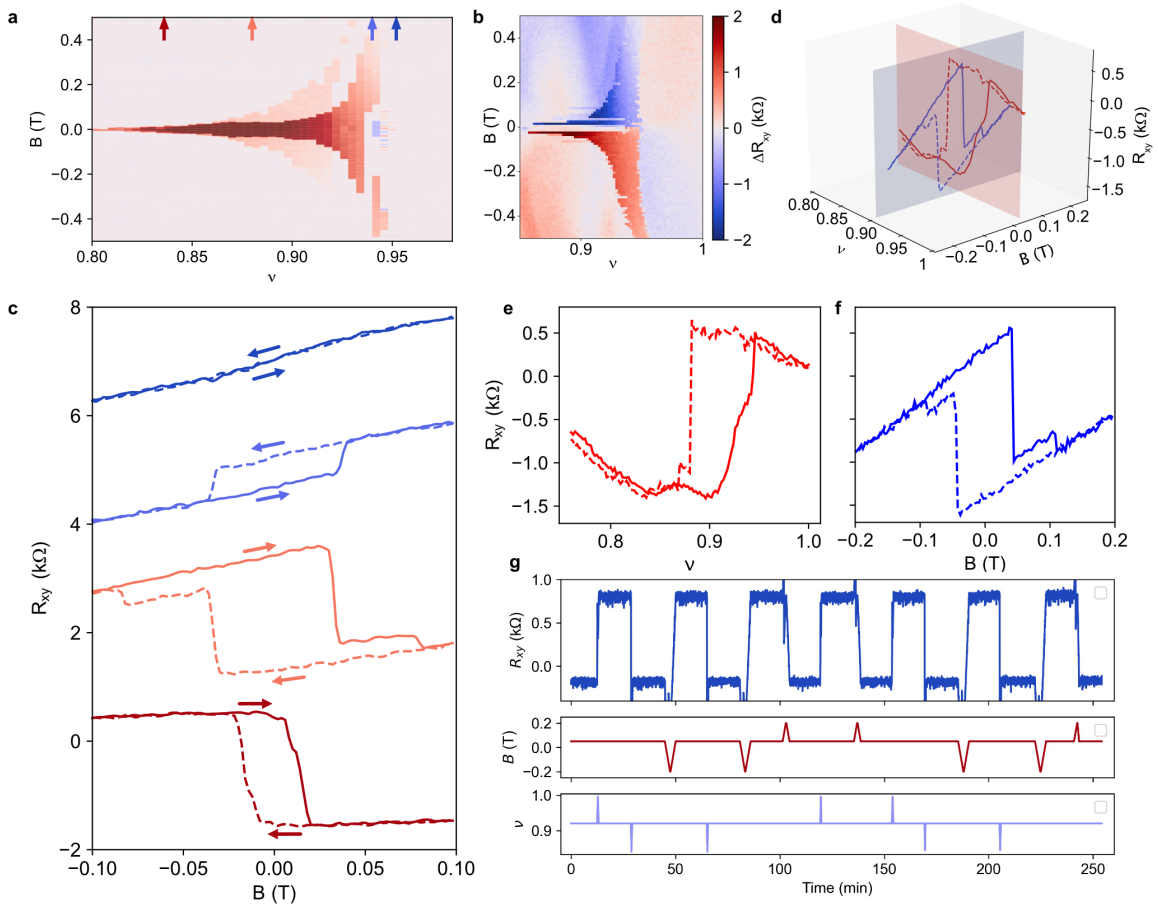
Supplementary Figure 4. **Charge-neutrality point disorder measurement.** The disorder in monolayer graphene is commonly measured using the width of the charge neutrality peak δn . The full-width half-max used for this plot is shown in the inset for the 1.10° data point with T_c of 1.59 K (red) and the 1.23° point (pink). However, we did not observe a correlation between superconducting T_c and the disorder measured using this method for TBG. Listed next to each data point is the maximum T_c measured for the twist angle, and the color corresponds to whether the superconductivity was on the hole (blue) or electron (red) side.

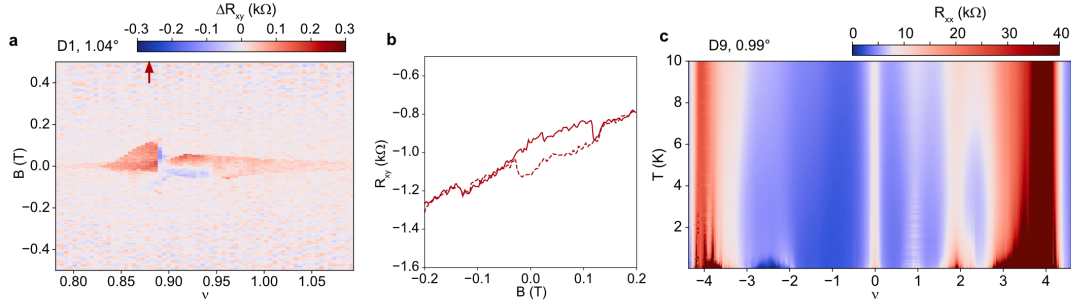


Supplementary Figure 5. **$d\rho/dT$ diagrams for devices of different angles.** **a-g**, Derivatives of resistivity with respect to temperature up to 40 K for twist angles from 0.95° to 1.23° . **h**, Selected linecuts of R_{xx} vs. temperature for the 1.04° twist angle (filling factor values also shown as coloured lines in **d**). The linecuts show the broad positive-curvature zone near charge neutrality (black line), the linear resistivity that persists down to a few Kelvin (although often blocked by a correlated insulator, superconducting, or other symmetry-broken state at low temperatures) near $|\nu| = 2$ (red and blue lines), and the super-linear low temperature to sub-linear high temperature states at $|\nu| > 2$ (purple and orange lines), which have large transition regions that prevent linear behavior until high temperatures. The curve at $\nu = -2.826$ (purple) shows an example where the higher-temperature positive-curvature zone is seen as the superconducting dome is phasing out (small T_c).

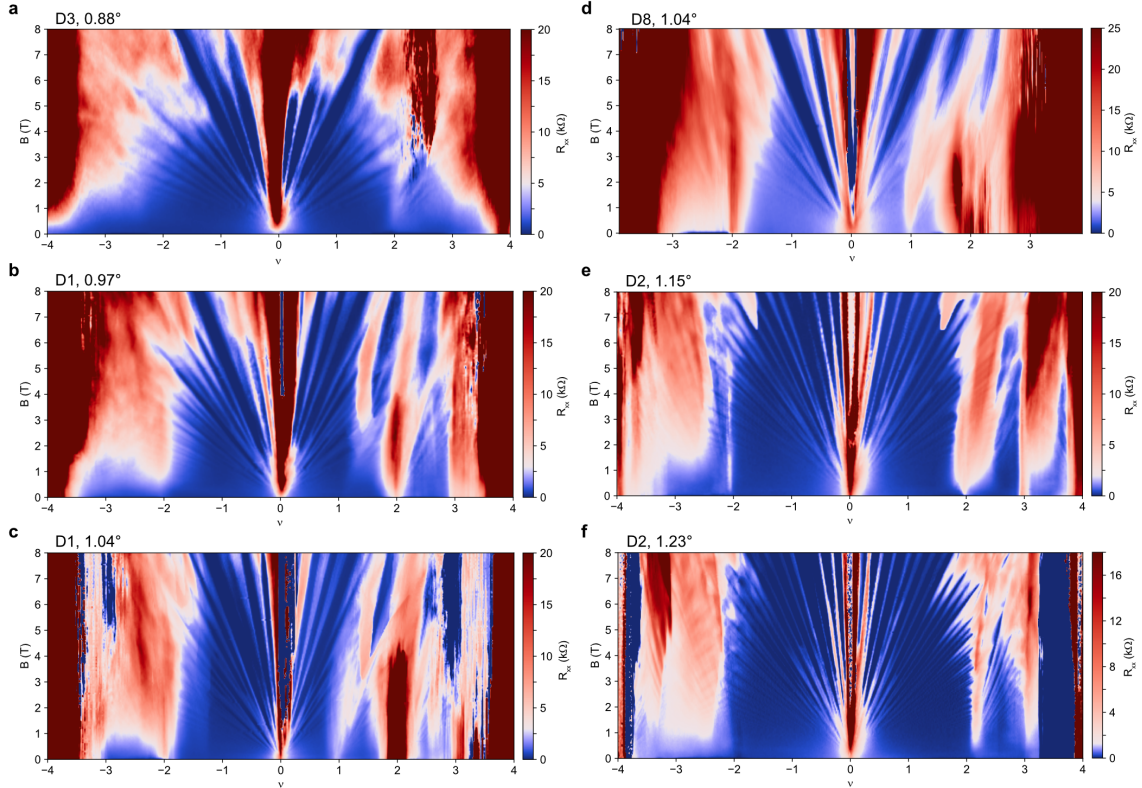


Supplementary Figure 6. R_{xx} Landau Fans and comparison of D1, 1.10° and D4, 1.10° **a, c**, R_{xx} and R_{xy} versus filling factor and magnetic field up to 8 T for D1. **b**, Schematics showing correlated Chern insulators (bold blue lines) and zero-field competing Chern insulators (red lines) at the magic angle. **d**, Hall conductance showing well-quantized Chern insulators emanating from charge neutrality (broadest plateaus at $C = \pm 4$, $\nu = \pm 1$ ($C = \pm 3$) and $\nu = \pm 2$ ($C = \pm 2$)). **e, f**, Landau fan of D4 and schematic of visible Landau levels along with correlated Chern insulators (bold lines). Notice the fan around charge neutrality does not show the usual clear 4-fold degeneracy preference represented by a wider Landau level plateau in **a**, and the fan emanating from $\nu = 1$ persists to lower fields. This variance in magnetic field dependence reveals the sensitivity of the symmetry-broken states near 1.10° , particularly near $\nu = 1$. **g, h**, T-dependence of D4 at high and low temperatures, respectively. Contrast this with the T-dependence of D1 in Fig. 3 and Supplementary Fig. 2.





Supplementary Figure 8. $\nu = 1$ **anomalous hall effect slightly away from magic angle**. **a**, ΔR_{xy} vs. B and ν around filling factor 1 measured with twist angle 1.04° in device D1 at 1.5K. **b**, Line cut of R_{xy} versus B at $\nu = 0.87$ (red arrow) for the same device. **c**, Temperature dependence of another device D9, twist angle 0.99° , showing evidence of switching behavior (similar to that seen in Fig. 3e) and therefore possible ferromagnetism near $\nu = 1$. Bad contacts prevented us from measuring R_{xy} data in this device.



Supplementary Figure 9. **Fan diagrams.** R_{xx} measured as a function of magnetic field B and moiré filling factor ν for a collection of twist angles. One can see high-resistance states near $\nu = 2$ just near the magic angle (0.97° to 1.15°) and near $\nu = 1$ only in a very small range near 1.10° (by 1.04° , it is already disappearing, and it is gone at 1.15° here). On the edge of the magic angle, (such as at 0.97°) the $\nu = 2$ state develops with a small magnetic field. The hole-side $\nu = -2$ insulator is always smaller than the electron-side $\nu = 2$ insulator, and it is not fully developed at 0 magnetic field in these diagrams. The noisy features commonly seen for $|\nu| > 3$ and occasionally for other values of ν at high field are likely due to contact/geometry effects near the insulating states.

Supplementary Table I. **Device table.** The superconducting transition temperatures (SC T_c), $\nu = 2$ correlated insulator (CI) gap, and $\nu = 1$ correlated state parameters measured for the devices used to plot the phase diagram in Fig. 1b,c sorted by twist angle.

Twist angle (± 0.02)	Device	Hole SC T_c (K)	Electron SC T_c (K)	$\nu=2$ CI (meV)	$\nu=1$ state
0.79	D6 (M20)	N/A	0.382	N/A	N/A
0.80	D7 (W5)	N/A	0.54	N/A	N/A
0.83	D6 (M20)	N/A	0.702	High-T peak	High-T peak
0.87	D6 (M20)	N/A	0.626	High-T peak	High-T peak
0.88	D3 (S3)	0.129	0.652	High-T peak	High-T peak
0.95	D9 (M30)	0.339	0.486	$\Delta=0.186$	High-T peak
0.97	D5 (M08)	0.742	0.089	$\Delta=0.68$	High-T peak
0.97	D1 (S13)	0.398	0.352	$\Delta=0.09$	High-T peak
0.99	D9 (M30)	0.429	N/A	$\Delta=0.11$	Low-T peak, switching
1.04	D1 (S13)	0.798	N/A	$\Delta=0.89$	Low-T peak, hysteresis
1.04	D8 (M12)	0.4	0.098	$\Delta=0.26$	Low-T peak
1.10	D1 (S13)	1.59	0.083	$\Delta=0.84$	FM to 7K
1.10	D4 (W3)	0.443	N/A	$\Delta=0.27$	Low-T peak
1.15	D2 (S12)	0.267	0.155	$\Delta \sim 0.17$ to SC	High-T peak
1.23	D2 (S12)	0.317	0.128	Disappearing	N/A

Pomeranchuk effect transition at $|\nu| \approx 1$

The phase transition at $|\nu| \approx 1$ has been previously explained as a transition from a fully flavor-symmetric Fermi liquid near charge-neutrality to a phase characterized by local free moments (approximately 1 per moire site) above $|\nu| \approx 1$ in analogy to the Pomeranchuk effect in He^3 ¹⁸. The free energy contribution due to the entropy of free spins is comparable with the contribution due to magnetic fields, so the phase transition line changes easily throughout the phase space of ν , B, and T. When considering the grand canonical potential approach, allowing the filling factor ν to change, and setting the magnetic field to zero, the phase transition line follows¹⁹:

$$\nu = \frac{1}{\Delta\mu} \left[-\frac{1}{2}\Delta\gamma T^2 - \ln(2)T + \Delta\epsilon \right] \quad (1)$$

This quadratic equation fits to the ν -T curves in Fig. 2 of the main text and provides the parameters plotted in panels Fig. 2c and Fig. 2d. $\Delta\mu$ represents the change in chemical potential between the Fermi liquid and isospin local moment phases, $\Delta\gamma$ is the change in the electronic specific heat (which is negative since the local moment phase has a smaller density of states), and $\Delta\epsilon$ is a free parameter related to a reference energies of the phases. A strong carrier density reset, and therefore strong correlations, are related to a strong $\Delta\mu$. Only the electron-side transitions were mapped in this study because they were detectable in a wider range of twist angles.

Theory: Ten-band model with onsite interaction

To model the interaction-induced symmetry breaking in twisted bilayer graphene (TBG), we take the non-interacting ten-band model for each flavor (spin, valley), and add interactions on top of it. Note that the correlation effects at charge neutrality for such system were modeled in a previous work,⁴² based on a single-flavor ten-band model with onsite interactions. In this work, we consider the four flavors (two spins, two valleys) altogether.

Single flavor

Let us recall that the ten-band model for a single flavor of electrons in TBG is realized on a triangular lattice with basis vectors $\mathbf{a}_1 = (\sqrt{3}/2, -1/2)$ and $\mathbf{a}_2 = (0, 1)$. We write the Bravais lattice sites as $\mathbf{r} = r_1\mathbf{a}_1 + r_2\mathbf{a}_2$ or simply as $\mathbf{r} = (r_1, r_2)$, where $r_{1,2} \in \mathbb{Z}$. Within each unit cell, there are ten orbitals which are distributed on three different sites. Explicitly, there are three orbitals, p_z , p_+ , and p_- , on every triangular lattice site. Each of the three kagome sites within a unit cell hosts an s orbital. Finally, both A and B sublattices of the honeycomb sites have p_+ and p_- orbitals. These are indicated and summarized in Supplementary Fig. 10.

Note that these ten orbitals should be regarded as Wannier orbitals which are able to faithfully produce the ten Bloch states closest to charge neutrality, including the two flat bands, while satisfying the same symmetry constraints of the original TBG system.

Throughout this work, we order the ten orbitals as

$$c_{\mathbf{r}} = (\tau_{z,\mathbf{r}}, \tau_{+,\mathbf{r}}, \tau_{-,\mathbf{r}}, \kappa_{1,\mathbf{r}}, \kappa_{2,\mathbf{r}}, \kappa_{2,\mathbf{r}}, \eta_{A+,\mathbf{r}}, \eta_{A-,\mathbf{r}}, \eta_{B+,\mathbf{r}}, \eta_{B-,\mathbf{r}})^T, \quad (2)$$

where τ , κ , and η denote operators on the triangular, kagome, and honeycomb sites respectively.

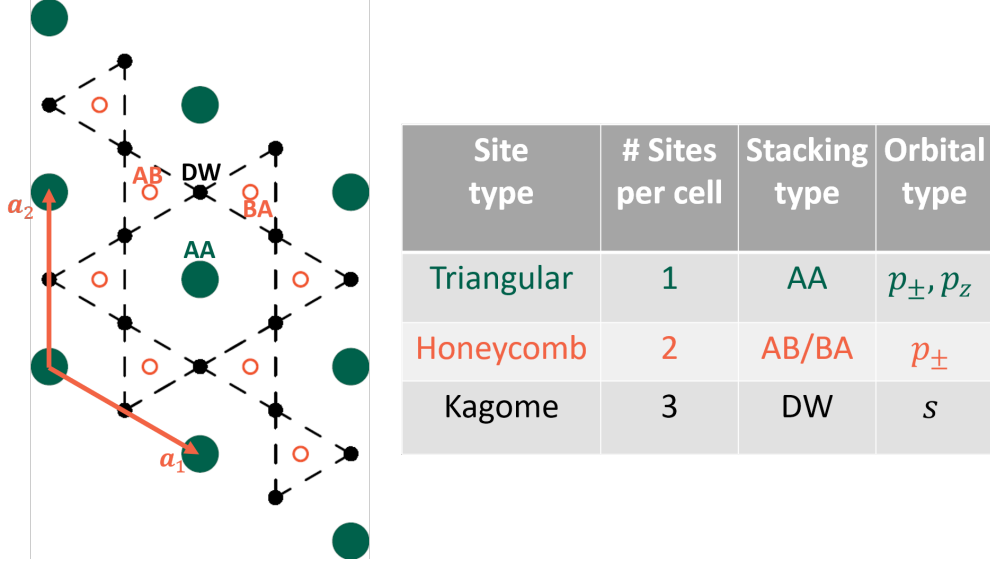
For the Hamiltonian of a single flavor (e.g. say $H_{K\uparrow}$, spin up in valley K), we took the same parameters as the ones in Ref.⁴²

Including spin and valley

The full non-interacting Hamiltonian including all flavors (spins and valleys) can be obtained in the following way. First, noting that the Hamiltonian does not explicitly depend on spin, in other words the Hamiltonians in both valleys have spin $SU(2)$ symmetry, we can, for each valley, simply duplicate the single-spin Hamiltonian to obtain the Hamiltonian for the two spin components. For example, the Hamiltonian for valley K is $H_K = H_{K\uparrow} \oplus H_{K\downarrow}$, with $H_{K\downarrow} = H_{K\uparrow}$.

Second, just as in monolayer graphene, the Hamiltonians at opposite valleys are related by the spinless time-reversal operation \mathcal{T} . Thus, we have the full Hamiltonian

$$H = H_K \oplus \mathcal{T}H_K\mathcal{T}^{-1}. \quad (3)$$



Supplementary Figure 10. **Lattice and orbitals for the ten-band model per flavor.** The green solid circles denote the triangular sites, corresponding to the AA stacking regions, with p_z , p_+ , and p_- orbitals. The red empty circles indicate the honeycomb sites, either type A or type B, corresponding to the AB/BA stacking regions, with p_+ and p_- orbitals on each of them. The black solid circles stand for the three types of kagome sites, which are the domain wall regions between the AB/BA regions. On each of these kagome sites, there is an s orbital.

Including interactions

We start from the general electron-electron interaction

$$H_{int} = \frac{1}{2} \sum_{\eta\eta'} \sum_{\sigma\sigma'} \int d\mathbf{r} d\mathbf{r}' \psi_{\eta\sigma}^\dagger(\mathbf{r}) \psi_{\eta'\sigma'}^\dagger(\mathbf{r}') V(\mathbf{r} - \mathbf{r}') \psi_{\eta'\sigma'}(\mathbf{r}) \psi_{\eta\sigma}(\mathbf{r}). \quad (4)$$

By projecting the interaction onto the subspace spanned by the ten (Wannier) orbitals of the ten-band model, and keeping only the onsite interaction on the triangular lattice sites, we obtained

$$H_{int} \simeq \sum_{\mathbf{r}} \sum_{\eta\eta'\sigma\sigma'} \sum_{m_1, m_2, m_3, m_4} V_{m_1 m_2 m_3 m_4}^{\eta\eta'} (\tau_{m_1, \mathbf{r}}^{(\eta\sigma)})^\dagger (\tau_{m_2, \mathbf{r}}^{(\eta'\sigma')})^\dagger \tau_{m_3, \mathbf{r}}^{(\eta'\sigma')} \tau_{m_4, \mathbf{r}}^{(\eta\sigma)}, \quad (5)$$

where η, η' are the valley indices, σ, σ' denote the spin, and $m_1, m_2, \dots = z, +, -$ label the three types of p orbitals on the triangular sites. The interaction matrix elements

$$V_{m_1 m_2 m_3 m_4}^{\eta\eta'} = \int d\mathbf{r} d\mathbf{r}' V(\mathbf{r} - \mathbf{r}') \phi_{m_1}^{(\eta)*}(\mathbf{r}) \phi_{m_2}^{(\eta')*}(\mathbf{r}') \phi_{m_3}^{(\eta')}(\mathbf{r}') \phi_{m_4}^{(\eta)}(\mathbf{r}), \quad (6)$$

where $\phi_m^{(\eta)}(\mathbf{r})$ is the wave function for the m -type p orbital for valley η . Here, we have assumed that these wave functions do not depend on spin, but they do depend on the valley indices according to

$$\phi_{\pm}^{(\eta)}(\mathbf{r}) = (\phi_{\mp}^{(-\eta)}(\mathbf{r}))^*, \quad \phi_z^{(\eta)}(\mathbf{r}) = (\phi_z^{(-\eta)}(\mathbf{r}))^*. \quad (7)$$

Because of the rotational symmetry of the p orbitals, the intra-valley interaction matrix elements can be parametrized in terms of two independent parameters U and J , as

$$V_{m_1 m_2 m_3 m_4}^{++} = U \delta_{m_1 m_4} \delta_{m_2 m_3} + J [\delta_{m_1 m_3} \delta_{m_2 m_4} + (-1)^{m_1+m_4} \delta_{-m_1 m_2} \delta_{-m_4 m_3}] = V_{m_1 m_2 m_3 m_4}^{--}, \quad (8)$$

where for p_z orbitals $m = 0$. On the other hand, the inter-valley interaction matrix elements can be parametrized by the same two parameters, as

$$V_{m_1 m_2 m_3 m_4}^{+-} = U \delta_{m_1 m_4} \delta_{m_2 m_3} + J [\delta_{-m_1 m_3} \delta_{m_2, -m_4} + (-1)^{m_1+m_4} \delta_{m_1 m_2} \delta_{m_4 m_3}] = V_{m_1 m_2 m_3 m_4}^{-+}. \quad (9)$$

In the current work, we set $J = 0$ for simplicity in the following. The interaction Hamiltonian in momentum space can be written as

$$H_{int} = \frac{U}{2V} \sum_{\eta} \sum_{\sigma\sigma'} \sum_{m_1 m_2} \sum_{\mathbf{k}_1 \mathbf{k}_2 \mathbf{q}} \left\{ \tau_{m_1}^{(\eta\sigma)\dagger}(\mathbf{k}_1) \tau_{m_2}^{(\eta\sigma')\dagger}(\mathbf{k}_2) \tau_{m_2}^{(\eta\sigma')}(\mathbf{k}_2 + \mathbf{q}) \tau_{m_1}^{(\eta\sigma)}(\mathbf{k}_1 - \mathbf{q}) \right. \\ \left. + \tau_{m_1}^{(\eta\sigma)\dagger}(\mathbf{k}_1) \tau_{m_2}^{(-\eta\sigma')\dagger}(\mathbf{k}_2) \tau_{m_2}^{(-\eta\sigma')}(\mathbf{k}_2 + \mathbf{q}) \tau_{m_1}^{(\eta\sigma)}(\mathbf{k}_1 - \mathbf{q}) \right\}, \quad (10)$$

where V is the volume of the system size. Now we apply the Hartree-Fock approximation. Up to a constant, we obtain the mean-field Hamiltonian

$$H_{int}^{HF} = \sum_{\eta\sigma} \sum_{\mathbf{k}} \sum_{m_1 m_2} \tau_{m_1}^{(\eta\sigma)\dagger}(\mathbf{k}) \tilde{W}_{m_1 m_2}^{\eta, \sigma} \tau_{m_2}^{(\eta\sigma)}(\mathbf{k}), \quad (11)$$

with

$$\tilde{W}_{m_1 m_2}^{\eta, \sigma} = U \left(\sum_{\eta'\sigma'} \text{Tr} P^{\eta', \sigma'} \delta_{m_1 m_2} - P_{m_1 m_2}^{\eta, \sigma} \right) \quad (12)$$

and

$$P_{m_1 m_2}^{\eta, \sigma} = \frac{1}{V} \sum_{\mathbf{k}'} \langle \tau_{m_2}^{(\eta\sigma)\dagger}(\mathbf{k}') \tau_{m_1}^{(\eta\sigma)}(\mathbf{k}') \rangle \quad (13)$$

It can be seen that the two terms in Eq. (12) can be identified as Hartree and Fock contributions, respectively.

In addition to the interaction, we assume there is a background positive charge distribution such that at charge neutrality the system is neutral. This potential can be modeled as

$$H_{bg} = -U \sum_{\mathbf{k}} \sum_{\eta'\sigma'} \text{Tr} P_{CN}^{\eta', \sigma'} \sum_{m\eta\sigma} \tau_m^{(\eta\sigma)\dagger}(\mathbf{k}) \tau_m^{(\eta\sigma)}(\mathbf{k}), \quad (14)$$

where $P_{CN}^{\eta, \sigma}$ is computed from the non-interacting Hamiltonian at charge neutrality. Thus, the total mean-field Hamiltonian can be written as

$$H = H_{nonint} + \sum_{\eta\sigma} \sum_{\mathbf{k}} \sum_{m_1 m_2} \tau_{m_1}^{(\eta\sigma)\dagger}(\mathbf{k}) \tilde{W}_{m_1 m_2}^{\eta, \sigma} \tau_{m_2}^{(\eta\sigma)}(\mathbf{k}) \quad (15)$$

with H_{nonint} the non-interacting ten-band model and

$$W_{m_1 m_2}^{\eta, \sigma} = \left(\sum_{\eta' \sigma'} U_H \text{Tr}(P^{\eta', \sigma'} - P_{C_N}^{\eta', \sigma'}) \delta_{m_1 m_2} - U_F P_{m_1 m_2}^{\eta, \sigma} \right), \quad (16)$$

which has to be determined self-consistently by diagonalizing H .

Note that here we have generalized the mean-field Hamiltonian by choosing two independent parameters U_H and U_F for the contributions due to the Hartree and Fock terms. These two parameters can be regarded as phenomenological parameters, similar to the Landau parameters in the Fermi liquid theory.

The energy per electron can be computed as

$$E = \sum_{\eta \sigma} \left\{ \frac{1}{V} \sum_{\mathbf{k}} \epsilon_{\eta, \sigma}(\mathbf{k}) - \frac{1}{2} \text{Tr} [\tilde{W}^{\eta, \sigma} P^{\eta, \sigma}] \right\}, \quad (17)$$

with

$$\tilde{W}^{\eta, \sigma} = U_H \sum_{\eta' \sigma'} \text{Tr} P^{\eta', \sigma'} \delta_{m_1 m_2} - U_F P_{m_1 m_2}^{\eta, \sigma}, \quad (18)$$

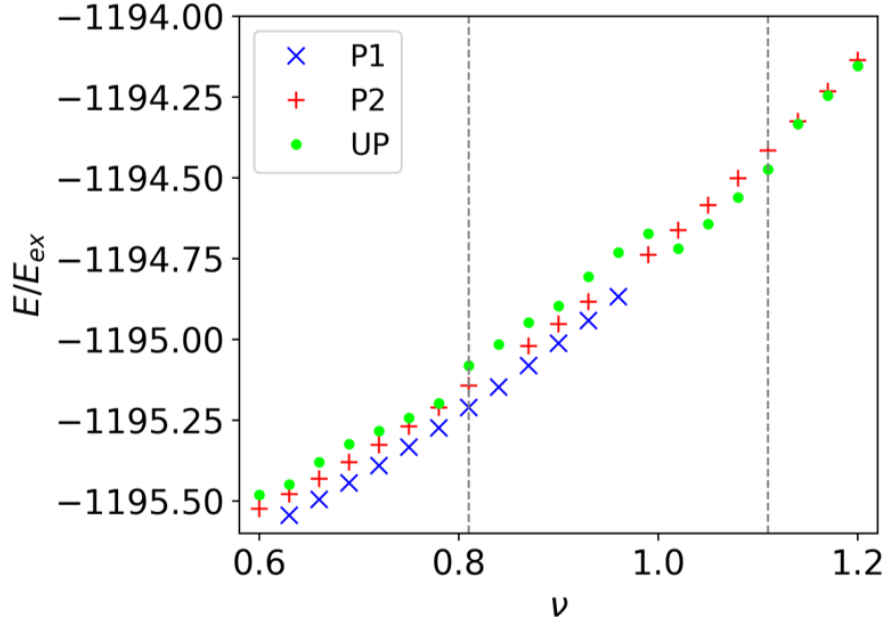
which generalizes Eq. (12) with independent Hartree and Fock contributions.

Competing states near $\nu = 1$

In this section, we show several possible phases that may exist near $\nu = 1$, based on the interacting ten-band model. In Supplementary Fig. 11, we show the ground state energy per electron for different phases.

Here, P1 and P2 states have maximal flavor polarization. Namely, the resulting state will be close to the configuration where each flavor, labeled by η, σ , is filled (depleted) sequentially above (below) charge neutrality. This is done by first adding this constraint to the self-consistent iterations until convergence is met. Then one relaxes the constraint and performs one additional iteration. The resulting state may not have the complete polarization on the maximally polarized flavor.

The UP state can also be a cascaded state. In this state, particularly, there are $[|\nu|]$ filled (depleted) flavors if $\nu > 0$ ($\nu < 0$), and the rest of the flavors will be filled (depleted) equally from charge neutrality (Here $[\cdot]$ denotes the truncated integer part of ν). In other words, the fractionally filled flavors will have equal filling fractions.



Supplementary Figure 11. **Ground state energies with filling.** Ground state energy per electron for different competing phases, near $\nu = 1$. The two dashed vertical lines indicate where the filling ν is 0.81 and 1.11, see also Supplementary Fig. 12 and Supplementary Fig. 14.

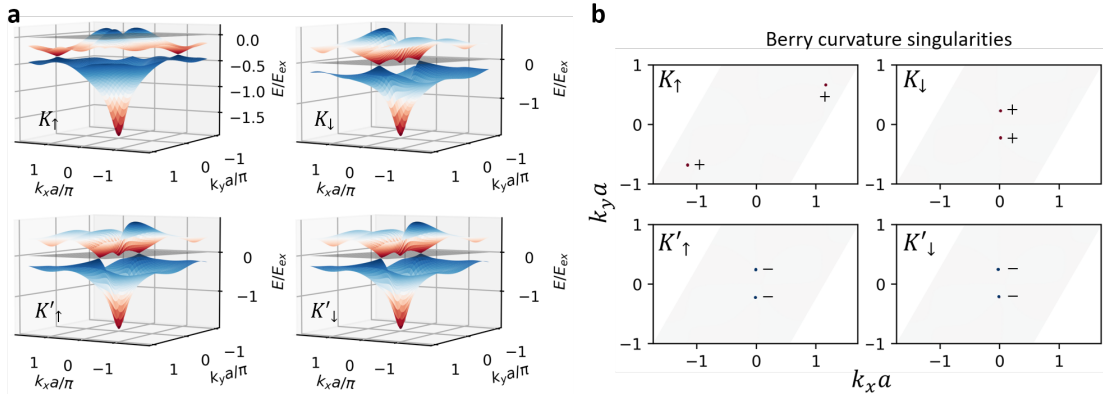
Energetically, from the Supplementary Fig. 11a, we see that the system prefers to be in the gapped P1 state, although the gapless P2 state is close in energy when $\nu < 1$, and it prefers to be in the UP state when $\nu > 1$. This coincides with the cascade picture previously proposed¹¹.

It is worth mentioning that due to the onsite nature of the interaction, there exist degeneracies when we consider different permutations of the filling fractions for different flavors. This means one can arbitrarily choose the flavors which are maximally polarized.

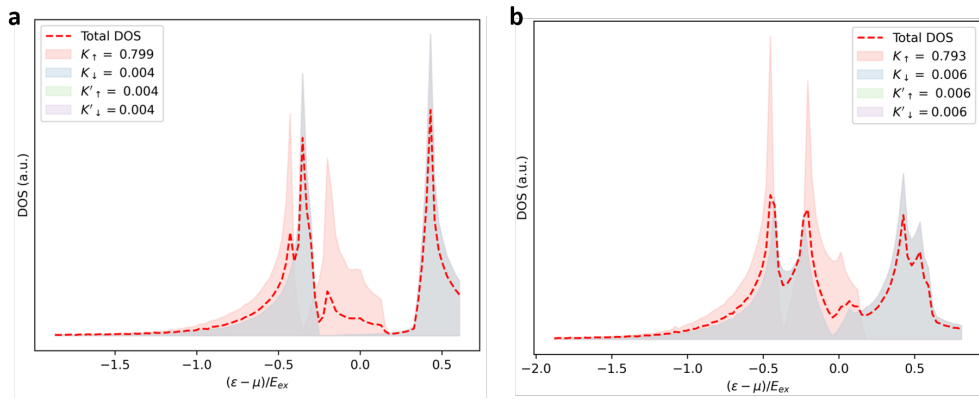
The P1 state has $C_2\mathcal{T}$ -broken gaps in the three flavors near charge neutrality. The band structures, as well as the Berry curvature, for this state at $\nu = 0.81$ are shown in Fig. 4 of the main text. The P2 state is gapless in all flavors. Moreover, for the fractionally filled flavors, C_3 symmetry is broken. The band structure of different flavors for the P2 state at $\nu = 0.81$ is shown in Supplementary Fig. 12, alongside the positions of the Dirac points, where the Berry curvature singularities are located. Because of this, the P2 state will not exhibit anomalous Hall effects, whereas the P1 state carries almost quantized Hall conductance since the Berry curvature is mostly distributed around the Γ point where the upper band bottom is located.

Supplementary Fig. 13, shows density of states for the P1 and P2 states.

In Supplementary Fig. 14, we show additional band structures and density of states, for UP states at $\nu = 0.81, 1.11$, and P2 state at $\nu = 1.11$. Here, the UP state at $\nu = 0.81$ has no flavor polarization and

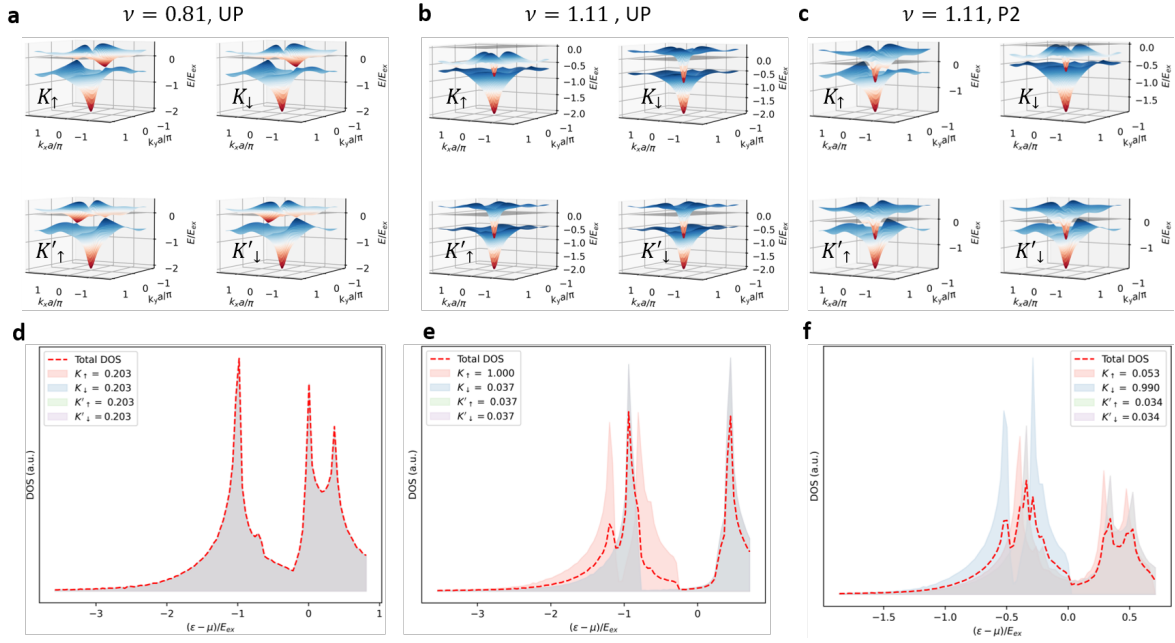


Supplementary Figure 12. **Theory of the gapless (P2) state.** **a**, Mean-field band structure obtained from the ten-band model for the case of broken $C_3\mathcal{T}$ symmetry at $\nu = 0.81$. **b**, Singularities of the Berry curvature Ω_{k_x, k_y} for the conduction flat band are located at the gapless points, as in **a**. The $+/-$ signs denotes the signs of the singularities, which are the same as the sign of the gapless Dirac nodes for each flavor.



Supplementary Figure 13. **Total and flavor-resolved density of states, at $\nu = 0.81$.** **a**, the $C_2\mathcal{T}$ -broken (P1) state. **b**, The C_3 -broken (P2) state. The fill colors each represent a spin/valley flavor, the gray color results from multiple flavors overlapping, and the red line is the normalized total density of states. The legends indicate the individual filling factor of each flavor.

carries zero Hall conductance. On the other hand, the UP state at $\nu = 1.11$ is after cascade, with one flavor almost filled and the rest three equally and partially filled. When the latter three flavors are filled slightly near the Γ pocket, they can still contribute to a finite Hall conductance for the reason similar to the one for the P1 state above. Finally, the P2 state for $\nu = 1.11$ cannot contribute to a nonzero Hall conductance.



Supplementary Figure 14. **Possible ground states near $\nu = 1$.** **a-c**, band structures. **d-f**, density of states. UP state at $\nu = 0.81$ (**a, d**). UP state at $\nu = 1.11$ (**b, e**). P2 state at $\nu = 1.11$ (**c, f**).